

Calculating phase-coherent quantum transport in nanoelectronics with *ab initio* quasiautomic orbital basis set

Xiaofeng Qian,^{1,*} Ju Li,² and Sidney Yip¹

¹*Department of Materials Science and Engineering and Department of Nuclear Science and Engineering, Massachusetts Institute of Technology, Cambridge, Massachusetts 02139, USA*

²*Department of Materials Science and Engineering, University of Pennsylvania, Philadelphia, Pennsylvania 19104, USA*

(Received 14 June 2010; published 23 November 2010)

We present an efficient and accurate computational approach to study phase-coherent quantum transport in molecular and nanoscale electronics. We formulate a Green's-function method in the recently developed *ab initio* nonorthogonal quasiautomic orbital basis set within the Landauer-Büttiker formalism. These quasiautomic orbitals are efficiently and robustly transformed from Kohn-Sham eigenwave functions subject to the maximal atomic-orbital similarity measure. With this minimal basis set, we can easily calculate electrical conductance using Green's-function method while keeping accuracy at the level of plane-wave density-functional theory. Our approach is validated in three studies of two-terminal electronic devices, in which projected density of states and conductance eigenchannel are employed to help understand microscopic mechanism of quantum transport. We first apply our approach to a seven-carbon atomic chain sandwiched between two finite cross-sectioned Al(001) surfaces. The emergence of gaps in the conductance curve originates from the selection rule with vanishing overlap between symmetry-incompatible conductance eigenchannels in leads and conductor. In the second application, a (4,4) single-wall carbon nanotube with a substitutional silicon impurity is investigated. The complete suppression of transmission at 0.6 eV in one of the two conductance eigenchannels is attributed to the Fano antiresonance when the localized silicon impurity state couples with the continuum states of carbon nanotube. Finally, a benzene-1,4-dithiolate molecule attached to two Au(111) surfaces is considered. Combining fragment molecular orbital analysis and conductance eigenchannel analysis, we demonstrate that conductance peaks near the Fermi level result from resonant tunneling through molecular orbitals of benzene-1,4-dithiolate molecule. In general, our conductance curves agree very well with previous results obtained using localized basis sets while slight difference is observed near the Fermi level and conductance edges.

DOI: [10.1103/PhysRevB.82.195442](https://doi.org/10.1103/PhysRevB.82.195442)

PACS number(s): 73.63.-b, 71.15.Ap, 73.22.-f

I. INTRODUCTION

The ongoing development of molecular and nanoscale electronics¹⁻⁸ is critical to the fabrication of solid-state devices that has followed the Moore's law for several decades. Single-molecule-based field-effect transistors, rectifiers, interconnects, and optical and mechanical switches may replace silicon in the post-complementary metal-oxide semiconductor (CMOS) devices and revolutionize information technology if such devices can be massively and cheaply fabricated and easily integrated. Molecular rectifier, known as the first conceptual molecular electronics, was proposed by Aviram and Ratner⁹ in the 1970s based on an organic donor-bridge-acceptor architecture. However, for decades such kind of molecular devices has not been synthesized, controlled, or measured, simply because single molecule is very sensitive to the chemical and dielectric environments, hence extremely hard to manipulate. Thanks to the tremendous success in experimental realizations and measurements at nanoscale, reproducible results of electrical conductance in molecular and nanoscale devices have finally been achieved during the last decade by mechanically controllable break junction,¹⁰⁻¹³ scanning tunneling microscope operated in the break junction regime,¹⁴⁻¹⁸ and spontaneous formation of molecular junctions,^{19,20} etc.

Elastic-scattering mean-free path of electrons in molecular and nanoscale devices is often larger than the size of conductor itself, reaching the phase-coherent regime of elec-

tron transport, which is beyond the present CMOS technology. A simple theoretical formula of electrical conductance for phase-coherent transport was proposed by Landauer²¹ and Büttiker,^{22,23} $G(E) = G_0 \mathcal{T}(E)$, which is the product of conductance quantum $G_0 = 2e^2/h$ ("2" accounts for spin degeneracy) and electron transmission probability $\mathcal{T}(E)$ at energy level E . Transmission probability \mathcal{T} can be obtained from the solution of single-particle quantum scattering problem and the magnitude of \mathcal{T} reflects scattering strength and interference characteristics when electrons pass through two- or multi-terminal devices. Clearly, the major assumption of the Landauer-Büttiker formalism is phase coherence. Recently, particular attention has also been devoted to inelastic-scattering effect²⁴⁻²⁸ which, on one hand, may cause local heating inside junctions and affect functionality and stability of devices. On the other hand, it was argued^{29,30} that the electron-phonon coupling could be one reason for negative differential resistance observed in experiments, thus the assumption of phase coherence has to be examined in the specific device that one is interested in. The Landauer-Büttiker formalism also assumed the absence of electron correlation. Meir and Wingreen³¹ extended the original formula in a more general one which considers current passing through a conductor containing interacting electrons instead of noninteracting ones. The generalized Landauer-Büttiker formula scales the original one by a self-energy correction due to electron correlations in the conductor region. Such effect was studied in the recent work by Ferretti *et al.*^{32,33} in one-dimensional molecular junctions.

During the past 20 years, computational approaches at the *ab initio* level for phase-coherent quantum transport have been extensively developed within the Landauer-Büttiker formalism, including equilibrium and nonequilibrium Green's function (NEGF) methods,^{34–47} Lippmann-Schwinger scattering-state approach,^{48–54} and layer Korrington-Kohn-Rostoker approach.⁵⁵ In practice NEGF method is often constructed on top of single-particle theories such as density-functional theory (DFT),^{56,57} and Hartree-Fock (HF) theory, neither of which include full quasiparticle physics in electron transport. As a consequence, DFT usually underestimates energy gap of semiconductors and insulators while very often HF overestimates it due to the missing correlation effect. It has been shown very recently that quasiparticle self-energy correction from many-body perturbation theory obtained using Hedin's GW approximation⁵⁸ greatly improves the description of electronic gap between occupied and unoccupied frontier adsorbate states, therefore drastically lowers theoretical electrical conductance toward experimental results.^{59–61} An alternative approach, time-dependent DFT,⁶² has also been proposed to include electron-electron correlation into quantum transport.^{63–67}

Practically speaking, DFT-NEGF and HF-NEGF calculations of electrical conductance in the full Hilbert space are not only computationally very demanding, but also unnecessary in most cases, due to the fact that almost all molecules and solids in nanoscale devices can be well described by low-energy physics. In other words, electron wave functions in molecules and solids do not deviate much from linear combination of atomic orbitals (LCAO).⁶⁸ Therefore, in the spirit of LCAO, localized basis sets are frequently adopted in standard NEGF calculations, including Slater-type orbitals (STO), Gaussian-type orbitals (GTO),⁶⁹ and localized pseudoatomic orbitals^{70,71} while STO and GTO have been extensively used in quantum chemistry community for decades. Consequently, Hamiltonian and overlap matrices are also strictly localized in real space, which makes direct and fast calculations of Green's function and self-energy possible. Nonetheless, one question is often asked: *are the localized basis sets used in NEGF calculations large enough to represent the Hilbert subspace of those low-energy single-particle states which are important for both ground-state electronic structure and electron transport?* The question can only be addressed by directly comparing results from both localized basis sets and plane-wave basis, the latter being continuously tunable and spatially homogeneous. However, the size of Hamiltonian in plane-wave basis is orders of magnitude larger than the one in localized basis sets, which makes direct inversion of Hamiltonian formidable. Fortunately, maximally localized Wannier functions (MLWFs) proposed by Marzari and Souza and Vanderbilt,^{72,73} adopting the quadratic spread localization measure,⁷⁴ paved a unique and elegant way to provide an exact mapping of Hilbert space spanned by Kohn-Sham wave functions inside particular energy window in a minimal basis. Green's-function method using the MLWF basis has become a rigorous approach^{75–79} to calculate zero-bias electrical conductance at the accuracy of plane-wave DFT. Recently Strange *et al.*⁸⁰ carried out a detailed comparison of conductance in a couple of nanoscale systems using both MLWFs from plane-wave

DFT calculations and numerical atomic orbitals from LCAO calculations. It was shown that LCAO calculations using the double-zeta polarized (DZP) basis agree very well with MLWF calculations while the single-zeta (SZ) and SZ polarized (SZP) basis sets give rise to large deviations. However, from transmission curves it was also clearly observed that even with DZP basis the energy positions of transmission peaks in LCAO calculations deviate from the ones obtained by MLWF calculations, especially the deep valence levels, indicating the insufficiency of these numeric SZ, SZP, and DZP basis sets. Despite tremendous success of MLWF approach, there is no closed-form solution for MLWFs, therefore iterative numerical procedures have to be adopted to find the global minimum. Furthermore, the center and shape of MLWFs are unknown until the iterative minimization of quadratic spread is fully finished.

Alternatively, we have recently developed an efficient and robust method⁸¹ to transform Bloch wave functions obtained from DFT calculations into a set of highly localized nonorthogonal quasiautomatic orbitals (QOs), which are maximally similar to the Bloch subspace spanned by pseudoatomic orbitals. Compared to the original quasiautomatic-minimal-basis-orbital (QUAMBO) method by Lu *et al.*,⁸² the current method not only arrives at the maximally similar orbitals, but also avoids the problem of bad condition number due to the unoccupied Bloch subspace truncation error. QOs and the associated *ab initio* tight-binding (TB) Hamiltonian and overlap matrices can accurately reproduce all the electronic structure information up to a few electron volts above the Fermi level. More importantly, explicit calculation of unoccupied states is avoided by resorting to resolution-of-the-identity property of Bloch space, hence dramatically reduces both computational effort and storage requirement. Taking advantages of the corresponding TB Hamiltonian and overlap matrices, efficient and accurate calculations of band structure, Fermi surface, and Mülliken charge and bond order have been carried out for isolated molecules, semiconductors, and metals. Therefore, similar to MLWFs, QOs can naturally serve as a minimal basis set for Green's-function method to study electron transport. In this work, we describe an efficient and accurate computational approach⁸³ to study phase-coherent quantum transport in molecular and nanoscale electronics within the Landauer-Büttiker formalism which retains the accuracy at the plane-wave DFT level.

This paper is organized as follows: in Sec. II Green's-function method with nonorthogonal localized basis for phase-coherent quantum transport is briefly introduced. In Sec. III we summarize our previous work on constructing nonorthogonal QOs from plane-wave DFT calculations. In Sec. IV Green's-function method in the QO basis set is applied to three cases: (a) a seven-carbon atomic chain sandwiched between two Al(001) surfaces with finite cross section, (b) a (4,4) single-wall carbon nanotube (CNT) with substitutional silicon impurity, and (c) benzene-1,4-dithiolate (BDT) molecule attached to two Au(111) surfaces. Calculated conductance is in very good agreement with other NEGF results obtained using localized basis sets while slight difference is found near the Fermi level and conductance edges. In addition, conductance eigenchannel analysis is performed to help understand microscopic mechanism of elec-

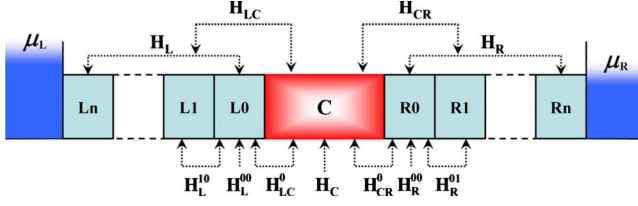


FIG. 1. (Color online) Schematic representation of two-terminal quantum transport device: two semi-infinite leads (light blue) connect the conductor (red) to the reservoirs (blue) characterized by electronic chemical potential μ_L and μ_R , respectively, in the semi-infinite limit. For the sake of efficient surface Green's function calculation, semi-infinite leads are further divided into periodic principal layers (L0, L1, ..., Ln; R0, R1, ..., Rn) as small as possible while ensuring negligible interaction between the principal layer and its second nearest principal layers under localized basis set. The conductor region has to also be chosen large enough to ensure vanishing coupling between left and right leads. For nonorthogonal localized basis set, there exists a similar schematic plot for overlap matrix \mathbf{S} .

tron transport in both devices. Finally, we summarize our work in Sec. V. Relevant information of the program and calculations is placed at a publicly accessible website.⁸³

II. GREEN'S-FUNCTION METHOD FOR PHASE-COHERENT QUANTUM TRANSPORT

A. Two-terminal quantum transport device

Two-terminal quantum transport device is represented by standard structure:^{35,40} left electron reservoir (μ_L)—left lead (L)—conductor (C)—right lead (R)—right electron reservoir (μ_R), as shown in Fig. 1. Hamiltonian of the whole device without reservoirs is simply written as

$$\mathbf{H} = \mathbf{H}_L + \mathbf{H}_{CL} + \mathbf{H}_C + \mathbf{H}_{CR} + \mathbf{H}_R. \quad (1)$$

\mathbf{H}_C , \mathbf{H}_L , and \mathbf{H}_R are Hamiltonians for conductor and left and right semi-infinite leads, and \mathbf{H}_{CL} (\mathbf{H}_{CR}) is coupling matrix between conductor and left (right) lead. Although the dimension of both leads is semi-infinite, Hamiltonians in nonorthogonal localized basis set for leads and conductor are localized sparse matrices. More explicitly, nonvanishing off-diagonal terms of Hamiltonian \mathbf{H} in Eq. (1) are very close to the diagonal terms owing to finite spatial range of localized-orbital basis. This localization feature allows fast matrix inversion and thus efficient self-energy and conductance calculations, which will be explained below. First, the conductor region should be large enough to make sure no interaction between left and right leads. Second, the semi-infinite leads are further divided into periodic principal layers⁸⁴ along transport direction. Here Hamiltonian for principal layers in the left (right) lead is denoted by \mathbf{H}_L^i (\mathbf{H}_R^i), where $i=0, 1, 2, \dots, \infty$. Principal layer is chosen to be as small as possible while ensuring the interaction between the i th principal and the $[i \pm n]$ th principal layer, $\mathbf{H}_R^{i \pm n}$, is negligible for $n \geq 2$. Thus, only $\mathbf{H}_L^{i \pm 1}$ ($\mathbf{H}_R^{i \pm 1}$) needs to be considered. Furthermore, due to the periodic structure of principal layers in the left and right leads, Hamiltonian for each principal layer

and coupling matrix between any two adjacent principal layers are also periodic. That means $\mathbf{H}_L^{i,i-1} = \mathbf{H}_L^{10} = (\mathbf{H}_L^{01})^\dagger = (\mathbf{H}_L^{i-1,i})^\dagger$, and $\mathbf{H}_R^{i,i-1} = \mathbf{H}_R^{10} = (\mathbf{H}_R^{01})^\dagger = (\mathbf{H}_R^{i-1,i})^\dagger$. Finally, a similar requirement applies to the interaction between the conductor and its adjacent principal layers so that \mathbf{H}_{CL}^i and \mathbf{H}_{CR}^i will be nonzero for $i=0$ only. In the nonorthogonal basis, one also needs to make sure the same conditions are satisfied for overlap matrix \mathbf{S} .

B. Conductance within the Landauer-Büttiker formalism

To calculate conductance in phase-coherent transport we apply Green's-function method^{31,34} within the Landauer-Büttiker formalism,²¹⁻²³ given in the following equation:

$$G(E) = G_0 T(E) = \frac{2e^2}{h} \text{Tr}[\Gamma_L \mathbf{G}_C^a \Gamma_R \mathbf{G}_C^r]. \quad (2)$$

Here G_0 stands for conductance quantum and $G_0 = 2e^2/h$ (2 accounts for spin degeneracy). “Tr[]” is the trace of matrix in the bracket and \mathbf{G}_C^r and \mathbf{G}_C^a are the retarded and advanced Green's functions of conductor at energy E . $\Gamma_{\{L,R\}}$ represents the coupling between conductor and leads,

$$\Gamma_{\{L,R\}} \equiv i(\Sigma_{\{L,R\}}^r - \Sigma_{\{L,R\}}^a), \quad (3)$$

where $\Sigma_{\{L,R\}}^r$ and $\Sigma_{\{L,R\}}^a$ are retarded and advanced self-energy corrections to conductor Hamiltonian due to its coupling with left and right semi-infinite leads. A simple relationship exists for retarded and advanced Green's function and self-energy, that is,

$$\mathbf{G}_C^r = (\mathbf{G}_C^a)^\dagger, \quad \Sigma_{\{L,R\}}^r = (\Sigma_{\{L,R\}}^a)^\dagger. \quad (4)$$

Correspondingly, total current passing through the leads is the integration of conductance over energy,

$$I = \frac{2e}{h} \int dE [f(E - \mu_L) - f(E - \mu_R)] T(E), \quad (5)$$

where f is Fermi distribution of electrons. As seen from the above equations, two key quantities, \mathbf{G}_C^r and $\Sigma_{\{L,R\}}^r$, are required for conductance calculations.

Following the schematic setup shown in Fig. 1 we can simplify infinite full Hamiltonian \mathbf{H} and its Green's function. Explicit forms of full Hamiltonian \mathbf{H} and overlap matrix \mathbf{S} in terms of conductor and leads are

$$\mathbf{H} = \begin{pmatrix} \mathbf{H}_L & \mathbf{H}_{CL}^\dagger & 0 \\ \mathbf{H}_{CL} & \mathbf{H}_C & \mathbf{H}_{CR} \\ 0 & \mathbf{H}_{CR}^\dagger & \mathbf{H}_R \end{pmatrix}, \quad \mathbf{S} = \begin{pmatrix} \mathbf{S}_L & \mathbf{S}_{CL}^\dagger & 0 \\ \mathbf{S}_{CL} & \mathbf{S}_C & \mathbf{S}_{CR} \\ 0 & \mathbf{S}_{CR}^\dagger & \mathbf{S}_R \end{pmatrix}.$$

Retarded Green's function \mathbf{G}^r of Hamiltonian is defined as $(z\mathbf{S} - \mathbf{H})\mathbf{G}^r = \mathbf{I}$ with $z = E + i\eta$ and η is an infinitesimal positive number. Its expanded form is written as

$$(z\mathbf{S} - \mathbf{H}) \begin{pmatrix} \mathbf{G}_L^r & \mathbf{G}_{LC}^r & \mathbf{G}_{LR}^r \\ \mathbf{G}_{CL}^r & \mathbf{G}_C^r & \mathbf{G}_{CR}^r \\ \mathbf{G}_{RL}^r & \mathbf{G}_{RC}^r & \mathbf{G}_R^r \end{pmatrix} = \begin{pmatrix} \mathbf{I}_L & 0 & 0 \\ 0 & \mathbf{I}_C & 0 \\ 0 & 0 & \mathbf{I}_R \end{pmatrix}. \quad (6)$$

Due to the short-ranged Hamiltonian and overlap matrices, \mathbf{G}_{LR}^r and \mathbf{G}_{RL}^r of direct couplings are negligible. We then

have the following solution for retarded Green's function \mathbf{G}_C^r of conductor:

$$\mathbf{G}_C^r = (z\mathbf{S}_C - \mathbf{H}_C - \Sigma_L^r - \Sigma_R^r)^{-1}, \quad (7)$$

where

$$\Sigma_L^r = (z\mathbf{S}_{CL} - \mathbf{H}_{CL})\mathbf{G}_L^r(z\mathbf{S}_{CL} - \mathbf{H}_{CL})^\dagger, \quad (8)$$

$$\Sigma_R^r = (z\mathbf{S}_{CR} - \mathbf{H}_{CR})\mathbf{G}_R^r(z\mathbf{S}_{CR} - \mathbf{H}_{CR})^\dagger, \quad (9)$$

$$\mathbf{G}_L^r = (z\mathbf{S}_L - \mathbf{H}_L)^{-1}, \quad (10)$$

$$\mathbf{G}_R^r = (z\mathbf{S}_R - \mathbf{H}_R)^{-1}. \quad (11)$$

As we have mentioned before, $\Sigma_{\{L,R\}}^r$ is the self-energy due to the coupling between conductor and leads, and they have the same dimension as \mathbf{H}_C and \mathbf{S}_C . Semi-infinite $\mathbf{G}_{\{L,R\}}^r$ is retarded Green's function of left and right leads. Notice that in the device setup $\mathbf{H}_{C\{L,R\}}^i = \mathbf{0}$ and $\mathbf{S}_{C\{L,R\}}^i = \mathbf{0}$ for $i \geq 1$ and this allows us to reduce $\Sigma_{\{L,R\}}^r$ into a more compact form. Here we take Σ_L^r as an example.

$$\begin{aligned} \Sigma_L^r &= \left(\begin{array}{cccc} \cdots & 0 & 0 & z\mathbf{S}_{CL}^0 - \mathbf{H}_{CL}^0 \\ \vdots & \vdots & \vdots & \vdots \\ \cdots & z\mathbf{S}_L^0 - \mathbf{H}_L^0 & z\mathbf{S}_L^{10} - \mathbf{H}_L^{10} & 0 \\ \cdots & z\mathbf{S}_L^{01} - \mathbf{H}_L^{01} & z\mathbf{S}_L^0 - \mathbf{H}_L^0 & z\mathbf{S}_L^{10} - \mathbf{H}_L^{10} \\ \cdots & 0 & z\mathbf{S}_L^{01} - \mathbf{H}_L^{01} & z\mathbf{S}_L^0 - \mathbf{H}_L^0 \end{array} \right)^{-1} \\ &\times \left(\begin{array}{c} \vdots \\ 0 \\ 0 \\ (z\mathbf{S}_{CL}^0 - \mathbf{H}_{CL}^0)^\dagger \end{array} \right) \\ &= (z\mathbf{S}_{CL}^0 - \mathbf{H}_{CL}^0)\mathbf{g}_L^0(z\mathbf{S}_{CL}^0 - \mathbf{H}_{CL}^0)^\dagger. \end{aligned} \quad (12)$$

Surface Green's function \mathbf{g}_L^0 of the principal layer L0 is extracted from semi-infinite retarded Green's function \mathbf{g}_L^r of the entire left lead. A similar expression for Σ_R^r can be directly obtained by changing "L" to "R" in the above formula. Moreover, surface Green's function \mathbf{g}_L^0 and \mathbf{g}_R^0 are calculated using an efficient iterative method proposed by Sancho *et al.*,⁸⁵⁻⁸⁷ in which 2^i principal layers are taken into account after the i th iteration.

C. Density of states

Density of states (DOS), $\rho_C(E)$, in the conductor region is closely related to the retarded Green's function $\mathbf{G}_C^r(E)$

$$\rho_C(E) = -\frac{1}{\pi} \text{Im}\{\text{Tr}[\mathbf{G}_C^r(E)\mathbf{S}_C]\}. \quad (13)$$

Im refers to the imaginary part of the value. The position-dependent DOS, $\rho_C(\mathbf{x}, E)$, is also easy to compute in any localized nonorthogonal basis set $\{e_m\}$,

$$\rho_C(\mathbf{x}, E) = -\frac{1}{\pi} \sum_{mn} \text{Im}[\mathbf{G}_C^r(E)]_{mn} e_n^*(\mathbf{x}) e_m(\mathbf{x}). \quad (14)$$

However we emphasize that DOS and local DOS (LDOS) from the above equations simply reflect the total number and

the detailed distribution of single-particle states at specific energy and position, respectively, and there is no exact one-to-one mapping between DOS/LDOS and electrical conductance. Localized standing waves, for example, do not contribute to conductance at all.

D. Conductance eigenchannels

Conductance calculated from Eq. (2) does not provide information of current distribution. It is thus unable to tell us deeper physics behind transport phenomena. For instance, how do vacancy and impurity in carbon nanotubes and graphene nanoribbons affect conductance? Why isomerization in molecular switches will lead to different conductances? What is the intrinsic reason for negative differential resistance (NDR)? Some of these questions can be answered roughly by chemical intuitions but not quantitatively and conclusively. Looking into the molecular and nanoscale electronics carefully, we can see that conductors and even leads are very often made of low-dimensional materials subject to quantum confinement. Low dimensionality and quantum confinement directly limit the number of molecular orbitals in conductors available near the Fermi level, hence limit the number of conductance channels. Conductance channels essentially come from the hybridization between molecular orbitals in conductors and delocalized Bloch states in leads. The above conceptual conductance eigenchannels have already been theoretically formulated and practically utilized.^{34,88} Presently it is one of the most powerful tools for understanding the role of chemical bonding and antibonding characteristics and determining microscopic transport mechanism with the help of modern visualization techniques.⁸⁹

One simple way to define conductance eigenchannels is to perform a singular value decomposition of the transmission matrix \mathbf{t} ,

$$\mathbf{U}_L \mathbf{t} \mathbf{U}_R^\dagger = \begin{pmatrix} \lambda_1 & 0 & \cdots \\ 0 & \lambda_2 & \cdots \\ \vdots & \vdots & \ddots \end{pmatrix}, \quad (15)$$

where $\mathbf{t} \equiv (\Gamma_R)^{1/2} \mathbf{G}_C^r (\Gamma_L)^{1/2}$ and \mathbf{U}_L and \mathbf{U}_R are unitary transformation matrices. As a result, total transmission is, $\mathcal{T}(E) = \sum_i \lambda_i^* \lambda_i$, using the cyclic invariance of trace

$$\mathcal{T}(E) = \text{Tr}(\Gamma_L \mathbf{G}_C^r \Gamma_R \mathbf{G}_C^r) = \text{Tr}(\mathbf{t}^\dagger \mathbf{t}). \quad (16)$$

However eigenchannels from the above approach are normalized in both flux and energy. Paulsson and Brandbyge proposed a different approach⁸⁸ which directly embed the information of transmission coefficient into its corresponding eigenchannel wave function. Such energy-normalized eigenchannels provide local DOS coming from conductance channels and can be directly compared with other eigenchannels. Here we briefly describe basic procedures proposed by Paulsson and Brandbyge⁸⁸ which is applied in our work under the QO basis set.

Spectral function \mathbf{A} of the conductor is defined by,

$$\mathbf{A}_C(E) = i(\mathbf{G}_C^r - \mathbf{G}_C^a) = \mathbf{G}_C^r(\mathbf{\Gamma}_L + \mathbf{\Gamma}_R)\mathbf{G}_C^a, \quad (17)$$

which is generated by incoming electron wave functions from both left and right leads. We focus on spectral function due to incoming electrons from the left lead, that is, $\mathbf{A}_L = \mathbf{G}_C^r \mathbf{\Gamma}_L \mathbf{G}_C^a$. Under the Löwdin orthogonalization, the corresponding spectral function is transformed into $\bar{\mathbf{A}}_L = \mathbf{S}^{1/2} \mathbf{A}_L \mathbf{S}^{1/2}$. Similarly, $\bar{\mathbf{\Gamma}}_R = \mathbf{S}^{-1/2} \mathbf{\Gamma}_R \mathbf{S}^{-1/2}$. Eigenvalues and eigenvectors of $\bar{\mathbf{A}}_L$ represent orthogonal scattering channels and the corresponding transmission coefficients in the conductor when electron propagates from left to right, that is,

$$\sum_n [\bar{\mathbf{A}}_L]_{mn} [\mathbf{U}]_{nl} = \lambda_l [\mathbf{U}]_{ml}. \quad (18)$$

The eigenvector contained in the unitary transformation matrix \mathbf{U} is then scaled by the corresponding transmission coefficient λ as follows:

$$[\tilde{\mathbf{U}}]_{ml} = \sqrt{\frac{\lambda_l}{2\pi}} [\mathbf{U}]_{ml}. \quad (19)$$

Transmission matrix under the above orthogonal scattering channels reads

$$T_{l'l} = 2\pi [\tilde{\mathbf{U}}^\dagger \bar{\mathbf{\Gamma}}_R \tilde{\mathbf{U}}]_{l'l}, \quad (20)$$

which is further diagonalized

$$\sum_n T_{mn} [\mathbf{C}]_{n\alpha} = \mathcal{T}_\alpha [\mathbf{C}]_{m\alpha}. \quad (21)$$

Here \mathcal{T}_α is transmission probability for eigenchannel α while $[\mathbf{C}]_{m\alpha}$ is the coefficient of Löwdin-orthogonalized orbital m in eigenchannel α . The corresponding eigenchannel in the conductor can be explicitly expressed in nonorthogonal basis set $\{|e_i\rangle\}$,

$$|\Phi_\alpha\rangle = \sum_i |e_i\rangle [\mathbf{S}^{-1/2} \tilde{\mathbf{U}} \mathbf{C}]_{i\alpha}. \quad (22)$$

$|\Phi_\alpha\rangle$ essentially represents eigenchannels with conductance amplitude embedded inside $|\Phi_\alpha\rangle$ itself. Probability current density $\mathbf{J}_\alpha(\mathbf{x})$ carried by eigenchannel $|\Phi_\alpha\rangle$ is simply

$$\mathbf{J}_\alpha(\mathbf{x}) = \frac{e}{2m} \{ \Phi_\alpha^* [(\mathbf{p} - e\mathbf{A})\Phi_\alpha] + \Phi_\alpha [(\mathbf{p} - e\mathbf{A})\Phi_\alpha^*] \}. \quad (23)$$

In the absence of external vector potential \mathbf{A} , we have

$$\mathbf{J}_\alpha(\mathbf{x}) = \frac{e\hbar}{m} \text{Im}[\Phi_\alpha^*(\mathbf{x}) \nabla \Phi_\alpha(\mathbf{x})]. \quad (24)$$

Since complex wave function $\Phi_\alpha(\mathbf{x})$ can be written as a product of its amplitude and phase, $\Phi_\alpha(\mathbf{x}) = |\Phi_\alpha(\mathbf{x})| \exp[i\phi_\alpha(\mathbf{x})]$, probability current density can be rewritten as

$$\mathbf{J}_\alpha(\mathbf{x}) = \frac{e\hbar}{m} \rho_\alpha(\mathbf{x}) \nabla \phi_\alpha(\mathbf{x}), \quad (25)$$

where $\rho_\alpha(\mathbf{x}) = |\Phi_\alpha(\mathbf{x})|^2$. Therefore, electron density $\rho_\alpha(\mathbf{x})$ and phase-gradient field $\nabla \phi_\alpha(\mathbf{x})$ are clearly two important components.

E. k-point sampling in the transverse Brillouin zone

In order to treat bulk electrodes, we need to take into account the periodic boundary condition (PBC) along two transverse directions. This can be achieved by forming Bloch functions e_{i,\mathbf{k}_\perp} of nonorthogonal basis set $\{|e_i\rangle\}$ at particular \mathbf{k}_\perp of the transverse Brillouin zone,

$$e_{i,\mathbf{k}_\perp}(\mathbf{x}) = \frac{1}{\sqrt{N_{L_\perp}}} \sum_{L_\perp} e_i(\mathbf{x} - \mathbf{X}_{L_\perp}) e^{i\mathbf{k}_\perp \cdot \mathbf{X}_{L_\perp}}, \quad (26)$$

where L_\perp runs through all unit cells on the transverse plane in the Born-von Kármán boundary condition and N_{L_\perp} is the total number of unit cells on the plane. The corresponding Hamiltonian and overlap matrices can be reformulated in the above Bloch functions,

$$H_{ij}(\mathbf{k}_\perp) \equiv \langle e_{i,\mathbf{k}_\perp} | \hat{H} | e_{j,\mathbf{k}_\perp} \rangle = \sum_{L_\perp} H_{ij}(L_\perp) e^{i\mathbf{k}_\perp \cdot \mathbf{X}_{L_\perp}} \quad (27)$$

and

$$S_{ij}(\mathbf{k}_\perp) \equiv \langle e_{i,\mathbf{k}_\perp} | \hat{S} | e_{j,\mathbf{k}_\perp} \rangle = \sum_{L_\perp} S_{ij}(L_\perp) e^{i\mathbf{k}_\perp \cdot \mathbf{X}_{L_\perp}}, \quad (28)$$

where $H_{ij}(L_\perp)$ corresponds to Hamiltonian matrix element between basis e_i at unit cell 0 and basis e_j at unit cell L_\perp . The size of Hamiltonian matrix $\mathbf{H}(\mathbf{k}_\perp)$ and overlap matrix $\mathbf{S}(\mathbf{k}_\perp)$ obtained from the Bloch transform is much smaller than the original matrices in the Born-von Kármán boundary condition. Conductance can be calculated at each \mathbf{k}_\perp -point using $\mathbf{H}(\mathbf{k}_\perp)$ and $\mathbf{S}(\mathbf{k}_\perp)$,

$$G(E, \mathbf{k}_\perp) = G_0 \text{Tr}[\mathbf{\Gamma}_L(\mathbf{k}_\perp) \mathbf{G}_C^a(\mathbf{k}_\perp) \mathbf{\Gamma}_R(\mathbf{k}_\perp) \mathbf{G}_C^r(\mathbf{k}_\perp)]. \quad (29)$$

Finally, the total conductance is the sum of weighted conductance at all \mathbf{k}_\perp points,

$$G(E) = \sum_{\mathbf{k}_\perp} w(\mathbf{k}_\perp) G(E, \mathbf{k}_\perp), \quad (30)$$

where $w(\mathbf{k}_\perp)$ is the weighting factor of \mathbf{k}_\perp in the transverse Brillouin zone.

III. QUASIAMORPHOUS ORBITALS

Here we briefly summarize the procedures of QO construction while more details can be found in our previous work.⁸¹ Our goal is to construct a set of localized QOs $\{Q_{li}\}$ to reproduce all DFT Kohn-Sham eigenvalues and eigenstates below an energy threshold E_{th} while these QOs are maximally similar to their corresponding AOs $\{A_{li}\}$. Q_{li} refers to the i th QO on atom l , where i contains principal (n), azimuthal (l), magnetic (m), and spin (σ) quantum numbers

of atomic orbitals. Since accurate description of electronic structure near the Fermi level is essential for transport calculations, this energy threshold E_{th} is often set to be a few electron volts above the Fermi level. These to-be-reproduced eigenstates satisfy the following Kohn-Sham equation:

$$\hat{H}|\psi_{n\mathbf{k}}\rangle = \varepsilon_{n\mathbf{k}}\hat{S}|\psi_{n\mathbf{k}}\rangle, \quad n = 1, \dots, R_{\mathbf{k}} \quad (31)$$

forming a finite-dimensional subspace $\mathcal{R}(\mathbf{k})$, where n and \mathbf{k} refer to Kohn-Sham states and the \mathbf{k} -point sampling in the first Brillouin zone, respectively. The positive definite Hermitian operator \hat{S} accounts for pseudowave-function augmentations in Vanderbilt's ultrasoft pseudopotentials. In the case of norm-conserving pseudopotentials it is simply the identity operator. The rest Bloch eigenstates that belong to infinite-dimensional subspace $\bar{\mathcal{R}}(\mathbf{k})$,

$$\hat{H}|\psi_{\bar{n}\mathbf{k}}\rangle = \varepsilon_{\bar{n}\mathbf{k}}\hat{S}|\psi_{\bar{n}\mathbf{k}}\rangle. \quad (32)$$

Different Bloch states are orthogonal to each other and $R_{\mathbf{k}}$ can vary with \mathbf{k} . The full Bloch space $\mathcal{B}(\mathbf{k})$ at \mathbf{k} point is the union of two subspaces: $\mathcal{B}(\mathbf{k}) \equiv \mathcal{R}(\mathbf{k}) \cup \bar{\mathcal{R}}(\mathbf{k})$.

To-be-reproduced Bloch states $\{\psi_{n\mathbf{k}}\}$ in $\mathcal{R}(\mathbf{k})$ themselves are not sufficient to construct QOs since the dimension of $\mathcal{R}(\mathbf{k})$ is usually smaller than the dimension of QOs. We, therefore, have to seek an optimized *combination* subspace $\mathcal{C}(\mathbf{k}) \subset \bar{\mathcal{R}}(\mathbf{k})$, consisting of *mutually orthonormal states* $\{c_{m\mathbf{k}}\}$, $m=1, \dots, C_{\mathbf{k}}$, to maximize the "sum-over-square" similarity measure \mathcal{L} , or the total sum of of AO projection squares onto the subspace defined by $\{\psi_{n\mathbf{k}}\}$ and $\{c_{m\mathbf{k}}\}$,

$$\begin{aligned} \mathcal{L} &\equiv \sum_{li} \left\| \left(\sum_{n\mathbf{k}} \hat{P}_{\psi_{n\mathbf{k}}} + \sum_{m\mathbf{k}} \hat{P}_{c_{m\mathbf{k}}} \right) |A_{li}\rangle \right\|^2, \\ &= \sum_{li} \left\| \hat{P}_{\{\psi_{n\mathbf{k}}\}} |A_{li}\rangle \right\|^2 + \left\| \hat{P}_{\{c_{m\mathbf{k}}\}} |A_{li}\rangle \right\|^2. \end{aligned} \quad (33)$$

\hat{P} is projection operator, defined by

$$\hat{P}_{\psi}|\phi\rangle \equiv \frac{(\psi, \phi)}{(\psi, \psi)}|\psi\rangle = \frac{\langle \psi | \hat{S} | \phi \rangle}{\langle \psi | \hat{S} | \psi \rangle} |\psi\rangle, \quad (34)$$

and $\hat{P}_{\{\psi_{n\mathbf{k}}\}} = \sum_{n\mathbf{k}} \hat{P}_{\psi_{n\mathbf{k}}}$. Optimized states $\{c_{m\mathbf{k}}\}$ are linear combinations of $\{\psi_{\bar{n}\mathbf{k}}\}$. $C_{\mathbf{k}} = qN - R_{\mathbf{k}}$, where q is the averaged number of AOs per atom and N is total number of atoms in the unit cell. The first part in Eq. (33) is the total sum-over-square projection of all AOs onto $\mathcal{R}(\mathbf{k})$, which is constant. Consequently we only need to focus on the second part Eq. (33) and optimize $\mathcal{C}(\mathbf{k})$ to maximize \mathcal{L} . Furthermore, \mathcal{L} does not depend on some part of $\bar{\mathcal{R}}(\mathbf{k})$ which has no overlap with Bloch subspace $\mathcal{A}(\mathbf{k})$ spanned by AOs. In another word, $\mathcal{C}(\mathbf{k})$ is a subset of the complement of $\mathcal{R}(\mathbf{k})$ within the union of $\mathcal{R}(\mathbf{k})$ and $\mathcal{A}(\mathbf{k})$, that is, $\mathcal{C}(\mathbf{k}) \subset \bar{\mathcal{A}}(\mathbf{k}) \equiv \{[\mathcal{R}(\mathbf{k}) \cup \mathcal{A}(\mathbf{k})] \setminus \mathcal{R}(\mathbf{k})\}$. The important consequence is that one can find $\mathcal{C}(\mathbf{k})$ from the *finite* complementary subspace $\bar{\mathcal{A}}(\mathbf{k})$ instead of constructing $\mathcal{C}(\mathbf{k})$ from the *infinite* $\bar{\mathcal{R}}(\mathbf{k})$ as proposed in the original QUAMBO method, while the final $\mathcal{C}(\mathbf{k})$ is exactly the same in both approaches as proved in our previous work.⁸¹

Bloch form of AO $|A_{li}\rangle$ at \mathbf{k} consists of a component that belongs to $\mathcal{R}(\mathbf{k})$, and a component that belongs to $\bar{\mathcal{R}}(\mathbf{k})$,

$$|A_{li,\mathbf{k}}\rangle = |A_{li,\mathbf{k}}^{\parallel}\rangle + |A_{li,\mathbf{k}}^{\perp}\rangle, \quad (35)$$

where

$$|A_{li,\mathbf{k}}^{\parallel}\rangle \equiv \sum_n \hat{P}_{\psi_{n\mathbf{k}}} |A_{li,\mathbf{k}}\rangle \quad (36)$$

and

$$|A_{li,\mathbf{k}}^{\perp}\rangle = |A_{li,\mathbf{k}}\rangle - \sum_n \hat{P}_{\psi_{n\mathbf{k}}} |A_{li,\mathbf{k}}\rangle. \quad (37)$$

$|A_{li,\mathbf{k}}^{\parallel}\rangle$ and $|A_{li,\mathbf{k}}^{\perp}\rangle$ can be calculated straightforwardly in plane-wave basis without knowing $\{\psi_{\bar{n}\mathbf{k}}\}$'s explicitly. We denote overlap matrix between $\{A_{li,\mathbf{k}}^{\perp}\}$ as $\mathbf{W}_{\mathbf{k}}$,

$$(\mathbf{W}_{\mathbf{k}})_{li,jj} = \langle A_{li,\mathbf{k}}^{\perp} | \hat{S} | A_{lj,\mathbf{k}}^{\perp} \rangle. \quad (38)$$

$\mathbf{W}_{\mathbf{k}}$ is a positive-semidefinite Gramian matrix. It can be diagonalized by a unitary matrix $\mathbf{V}_{\mathbf{k}}$ such that $\mathbf{W}_{\mathbf{k}} = \mathbf{V}_{\mathbf{k}} \mathbf{Y}_{\mathbf{k}} \mathbf{V}_{\mathbf{k}}^{\dagger}$, where $\mathbf{V}_{\mathbf{k}} \mathbf{V}_{\mathbf{k}}^{\dagger} = \mathbf{I}_{qN \times qN}$. The diagonal matrix $\mathbf{Y}_{\mathbf{k}}$ contains non-negative real eigenvalues. All the possible orthonormal states $\{c_{m\mathbf{k}}\}$ of combination subspace $\mathcal{C}(\mathbf{k})$ can be constructed using eigenvalues and eigenvectors of $\mathbf{W}_{\mathbf{k}}$ matrix,

$$|c_{m\mathbf{k}}\rangle = \sum_{li} (\bar{\mathbf{V}}_{\mathbf{k}})_{li,m} |A_{li,\mathbf{k}}^{\perp}\rangle, \quad (39)$$

where $(\bar{\mathbf{V}}_{\mathbf{k}})_{li,m} = (\mathbf{V}_{\mathbf{k}})_{li,m} (\mathbf{Y}_{\mathbf{k}})_{mm}^{-1/2}$. As a result, the sum-over-square measure \mathcal{L} defined in Eq. (33) can be rewritten in the following simple form:

$$\begin{aligned} \mathcal{L} &= \sum_{li} \left\| \sum_{\mathbf{k}} |A_{li,\mathbf{k}}^{\parallel}\rangle \right\|^2 + \sum_{\mathbf{k}} \text{Tr}(\mathbf{W}_{\mathbf{k}} \bar{\mathbf{V}}_{\mathbf{k}} \bar{\mathbf{V}}_{\mathbf{k}}^{\dagger} \mathbf{W}_{\mathbf{k}}) \\ &= \sum_{li} \left\| \sum_{\mathbf{k}} |A_{li,\mathbf{k}}^{\parallel}\rangle \right\|^2 + \sum_{m\mathbf{k}} (\mathbf{Y}_{\mathbf{k}})_{mm}. \end{aligned} \quad (40)$$

$\sum_m (\mathbf{Y}_{\mathbf{k}})_{mm}$ basically sums all $C_{\mathbf{k}}$ eigenvalues arbitrarily chosen from total qN non-negative real eigenvalues of $\mathbf{W}_{\mathbf{k}}$ matrix. Therefore, Eq. (40) suggests that we can maximize \mathcal{L} by choosing the largest $C_{\mathbf{k}}$ eigenvalues and their corresponding eigenvectors.

Once $\{c_{m\mathbf{k}}\}$ is chosen, we can merge basis functions in $\mathcal{R}(\mathbf{k})$ and $\mathcal{C}(\mathbf{k})$ together,

$$\{\phi_{n\mathbf{k}}\} = \{\psi_{n\mathbf{k}}\} \cup \{c_{m\mathbf{k}}\}. \quad (41)$$

More specifically, they are

$$\phi_{n\mathbf{k}} = \begin{cases} \psi_{n\mathbf{k}}, & n = 1, \dots, R_{\mathbf{k}} \\ c_{n\mathbf{k}}, & n = R_{\mathbf{k}} + [1, \dots, C_{\mathbf{k}}]. \end{cases}$$

Thus, $\{\phi_{n\mathbf{k}}\}$ consists of a qN -dimensional orthonormal basis for $\mathcal{Q}(\mathbf{k}) = \mathcal{R}(\mathbf{k}) \cup \mathcal{C}(\mathbf{k})$. We, therefore, can build up the full Hamiltonian matrix $\boldsymbol{\epsilon}_{\mathbf{k}}$ between any two functions in $\{\phi_{n\mathbf{k}}\}$, that is, $(\boldsymbol{\epsilon}_{\mathbf{k}})_{n,n'} \equiv \langle \phi_{n\mathbf{k}} | \hat{H} | \phi_{n'\mathbf{k}} \rangle$. Due to the fact that (a) $\{\psi_{n\mathbf{k}}\}$ are eigenfunctions of Kohn-Sham Hamiltonian, (b) $\{c_{m\mathbf{k}}\}$ are *not* eigenfunctions, and (c) $\{\psi_{n\mathbf{k}}\}$ and $\{c_{m\mathbf{k}}\}$ belong to different Bloch subspaces, we then have the following expression for $\boldsymbol{\epsilon}_{\mathbf{k}}$:

$$(\epsilon_{\mathbf{k}})_{n,n'} = \begin{cases} \epsilon_{n\mathbf{k}} \delta_{nn'}, & n, n' = 1, \dots, R_{\mathbf{k}} \\ \langle \phi_{n\mathbf{k}} | \hat{H} | \phi_{n'\mathbf{k}} \rangle, & n, n' = R_{\mathbf{k}} + [1, \dots, C_{\mathbf{k}}] \\ 0, & \text{otherwise.} \end{cases}$$

It is worth noting that in the above equation Kohn-Sham Hamiltonian \hat{H} has to be applied explicitly to obtain the matrix elements of $\epsilon_{\mathbf{k}}$ between two different $c_{m\mathbf{k}}$'s at the same \mathbf{k} . Finally, nonorthogonal QO is formed by

$$|Q_{ii}\rangle = \sum_{n\mathbf{k}} \hat{P}_{\phi_{n\mathbf{k}}} |A_{ii}\rangle = \sum_{n\mathbf{k}} (\Omega_{\mathbf{k}})_{n,ii} |\phi_{n\mathbf{k}}\rangle, \quad (42)$$

where $n=1, \dots, qN$, \mathbf{k} runs over $1, \dots, L_1 L_2 L_3$ Monkhorst-Pack grid, and

$$(\Omega_{\mathbf{k}})_{n,ii} \equiv \langle \phi_{n\mathbf{k}} | \hat{S} | A_{ii} \rangle \quad (43)$$

is a $qN \times qN$ matrix.

Under QO basis, real-space *ab initio* TB Hamiltonian $H_{ii,jj}(\mathbf{X}_L)$ between Q_{ii}^0 and Q_{jj}^L in two unit cells can be easily calculated as the following:

$$H_{ii,jj}(\mathbf{X}_L) \equiv \langle Q_{ii}^0 | \hat{H} | Q_{jj}^L \rangle = \sum_{\mathbf{k}} e^{-i\mathbf{k} \cdot \mathbf{X}_L} (\Omega_{\mathbf{k}}^\dagger \epsilon_{\mathbf{k}} \Omega_{\mathbf{k}})_{ii,jj}, \quad (44)$$

where $\mathbf{X}_L = l_1 \mathbf{a}_1 + l_2 \mathbf{a}_2 + l_3 \mathbf{a}_3$ is an integer combination of unit-cell edge vectors. Similarly, real-space overlap matrix $O_{ii,jj}(\mathbf{X}_L)$ can be obtained as

$$O_{ii,jj}(\mathbf{X}_L) \equiv \langle Q_{ii}^0 | \hat{S} | Q_{jj}^L \rangle = \sum_{\mathbf{k}} e^{-i\mathbf{k} \cdot \mathbf{X}_L} (\Omega_{\mathbf{k}}^\dagger \Omega_{\mathbf{k}})_{ii,jj}. \quad (45)$$

Clearly $H_{ii,jj}(\mathbf{X}_L)$ and $O_{ii,jj}(\mathbf{X}_L)$ have the similar localization property as QOs and should decay to zero as \mathbf{X}_L goes to infinity. With *ab initio* TB Hamiltonian and overlap matrices, we can efficiently compute eigenvalues at an arbitrary \mathbf{k} point (not necessarily one of $L_1 L_2 L_3$ \mathbf{k} points in DFT calculations), by forming

$$H_{ii,jj}(\mathbf{k}) = \sum_{|\mathbf{X}_L| \leq R_{\text{cut}}} e^{i\mathbf{k} \cdot \mathbf{X}_L} H_{ii,jj}(\mathbf{X}_L), \quad (46)$$

and

$$O_{ii,jj}(\mathbf{k}) = \sum_{|\mathbf{X}_L| \leq R_{\text{cut}}} e^{i\mathbf{k} \cdot \mathbf{X}_L} O_{ii,jj}(\mathbf{X}_L), \quad (47)$$

where \mathbf{X}_L runs over shells of neighboring unit cells with significant $H_{ii,jj}(\mathbf{X}_L)$ and $O_{ii,jj}(\mathbf{X}_L)$. Typically we determine a radial cut-off distance R_{cut} and sum only those elements satisfying $|\mathbf{X}_L| \leq R_{\text{cut}}$ in Eq. (46) and Eq. (47). Then, by solving the following generalized eigenvalue matrix problem,

$$\mathbf{H}(\mathbf{k})\Pi(\mathbf{k}) = \mathbf{O}(\mathbf{k})\Pi(\mathbf{k})\mathbf{E}(\mathbf{k}), \quad (48)$$

we obtain total qN eigenvalues in the diagonal matrix $\mathbf{E}(\mathbf{k})$ at each \mathbf{k} point. It is expected that, if $H_{ii,jj}(\mathbf{X}_L)$ and $O_{ii,jj}(\mathbf{X}_L)$ are strictly zero outside R_{cut} , all the $R_{\mathbf{k}}$ eigenvalues lower than energy threshold E_{th} are exactly the same as the eigenenergies obtained from DFT calculations. Therefore in practice, before building up lead and conductor Hamiltonian and overlap matrices for transport calculation, R_{cut} has to be

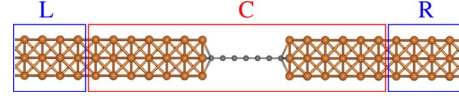


FIG. 2. (Color online) Atomic structure of Al(001)-C₇-Al(001) with finite cross section. L: principal layer in the left lead; C: conductor; R: principal layer in the right lead.

benchmarked by comparing TB and DFT band structures using the coarse \mathbf{k} sampling. On the other hand, this cutoff will be unnecessary if one is simply interested in a dense interpolation of electronic structure such as band structure, Fermi surface, and Fermi velocity. Consequently, the interpolated electronic structure will be very accurate and the original DFT eigenvalues $\epsilon_{n\mathbf{k}}$ from the coarse \mathbf{k} sampling will be exactly reproduced.

IV. APPLICATION

In the above section, we introduce an efficient method to construct localized QOs and their corresponding *ab initio* TB Hamiltonian and overlap matrices. With this localized basis set, Green's-function method based on the Landauer-Büttiker formalism can be applied to calculate electrical conductance of phase-coherent transport in molecular and nanoscale materials. We have implemented both QO method and equilibrium Green's-function method, as well as the interfaces to plane-wave DFT codes such as VASP,⁹⁰ DACAPO,⁹¹ and QUANTUM-ESPRESSO.⁹² Here we present three applications of our approach: (a) a seven-carbon atomic chain sandwiched between two Al(001) surfaces with finite cross-section: Al(001)-C₇-Al(001), (b) (4,4) CNT with substitutional silicon impurity, and (c) BDT molecule attached to two Au(111) surfaces: Au(111)-BDT-Au(111). Our result is shown to be consistent with other NEGF calculations. In addition, conductance eigenchannel analysis is performed to understand microscopic transport mechanism.

A. Al(001)-C₇-Al(001) with finite cross section

Atomic structure of Al(001)-C₇-Al(001) with finite cross section is illustrated in Fig. 2, which is the same structure as that used by others.^{41,46,53} The conductor is put inside a rectangular box of $14.0 \times 14.0 \times 34.238 \text{ \AA}^3$ and electrons transport along the $+z$ direction. The Al(001) lead is cut from fcc aluminum with lattice constant of 4.05 \AA and it consists of four atomic layers with 4-5-4-5 aluminum atoms from left to right. The distance between the edge carbon atom and the nearest 4-Al atomic plane is 1.0 \AA and the C-C bond length is 1.323 \AA . Both ends of carbon atomic chain are connected to 4-Al atomic planes. Under PBC, the above specific interface gives rise to different numbers of aluminum atomic layers in the left and right parts of the conductor. DFT calculations are performed in the QUANTUM-ESPRESSO package using the Perdew-Burke-Ernzerhof generalized-gradient approximation (PBE-GGA) of exchange-correlation functional,⁹³ a plane-wave basis with a cutoff of 400.0 eV , and ultrasoft pseudopotentials⁹⁴ for both aluminum and carbon atoms. Energy threshold E_{th} is set to 5.0 eV above the

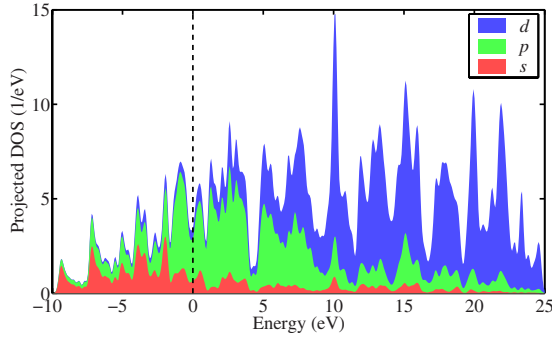


FIG. 3. (Color online) QO-projected DOS.

Fermi level for QO construction. Although valence electrons in single aluminum atom only occupy s and p AOs, s , p , and d AOs are strongly hybridized with each other near the Fermi level of metallic aluminum leads. Thus, we construct nine QOs (one s , three p , and five d -like QOs) for each aluminum atom and four QOs (one s and three p -like QOs) for each carbon atom. QO-projected DOS is shown in Fig. 3, which clearly demonstrates that five d -like QOs (indicated by the blue area in the upper part of QO-projected DOS curve) do not contribute much in the deep valence levels, however they have non-negligible contributions close to the Fermi level and as energy level further increases they become dominant beyond 10 eV above the Fermi level.

Band structure of Al(001) leads is shown in Fig. 4(a). Here four atomic layers are contained in a unit cell. *Ab initio* TB band structure (black-solid lines) using $R_{\text{cut}}=10$ Å agrees excellently with Kohn-Sham eigenvalues obtained from DFT calculation (red-filled dots) below $E=3.0$ eV. The slight deviation between 3.0 and 5.0 eV mainly comes from the diffusive nature of QOs in metallic aluminum leads. DOS and electrical conductance of Al(001) leads are shown in Fig. 4(b). We observe step-like conductance curve and sharp DOS peaks and they are the signature of perfect conductance channels in pristine conductors. The conductance steps indicate the maximum number of perfect conductance channels in the leads, which can also be obtained by counting number of bands crossing constant energy levels in the band structure plot.

Electrical conductance and DOS of Al(001)-C₇-Al(001) are presented in Figs. 5(a) and 5(b), respectively. We found very good agreement between our conductance curve and the ones calculated by Brandbyge *et al.* using TRANSIESTA package,⁴¹ Ke *et al.* using SIESTA,⁴⁶ and Smogunov *et al.* using scattering state approach.⁵³ However, a noticeable difference is observed in the conductance curves from localized basis set and plane-wave basis calculations.⁵³ Specifically, the localized basis-set calculations provide larger conductance near the Fermi level. Furthermore, the positions of conductance curve edges are slightly shifted. Our results, hence, demonstrate that in general NEGF using localized basis sets can offer accurate conductance curves, however, more attention has to be paid to choosing appropriate localized basis sets in order to achieve both accuracy and efficiency.⁸⁰

Furthermore, it is observed that total conductance is always no larger than $2 G_0$. From chemical intuition, perfect carbon atomic chain usually has two π orbitals near the

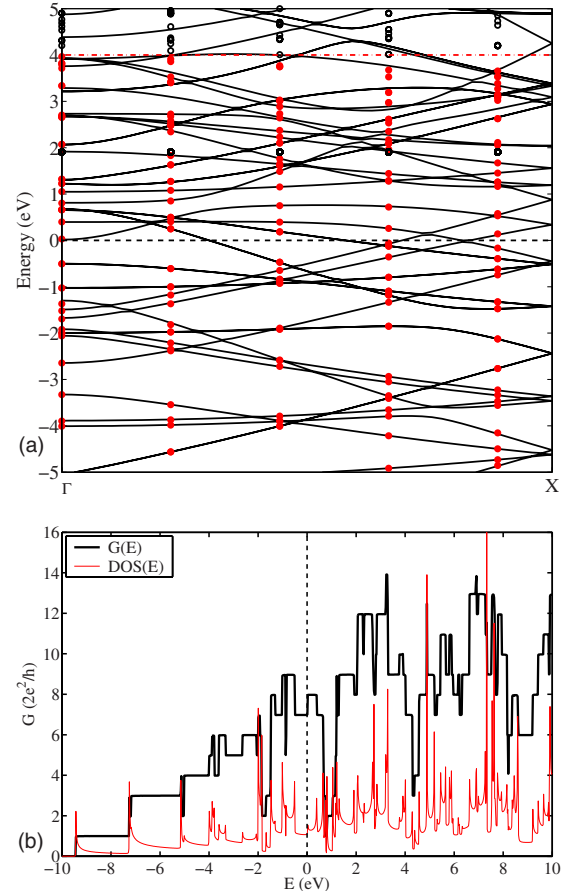


FIG. 4. (Color online) (a) Band structure (black-dashed line: the Fermi level; red dashed-dotted line: energy threshold; red-filled dots: DFT eigenvalues; black-open dots: DFT eigenvalues that are not used; black-solid line: *ab initio* TB band structure.) (b) DOS (red-thin line) and electrical conductance (black-thick line) of the Al(001) lead with $R_{\text{cut}}=10$ Å.

Fermi level formed by p_x and p_y orbitals perpendicular to the chain. Thus, it is likely that the maximum conductance of $2 G_0$ comes from two perfect conducting channels formed by these π orbitals. To examine this speculation, we perform conductance eigenchannel analysis at different energy levels which are listed in Table I. In this case, the incoming electrons propagate from left to right (along the $+\hat{z}$ direction). It is found that indeed the major channels are all doubly degenerate and each of them is either smaller than G_0 or close to G_0 depending on the energy. However, having conductance values of eigenchannels will not help us decode microscopic mechanism of transport phenomena. Actually all the detailed information is carried by eigenchannel itself. Therefore, we plot the corresponding eigenchannels in Fig. 6, whose phase amplitude is indicated by color using the color map shown in Fig. 7. In particular, red and cyan stand for the phase angle of $\pm\pi$ and 0, respectively, representing real wave functions.

Several features are immediately revealed from Fig. 6. First, it is clearly seen that electrons propagate through p_x - and p_y -like eigenchannels of carbon atomic chain, which confirms our previous speculation. Second, conductance channels at lower energy contain less nodes than those at higher energy. This is closely correlated with the distribution

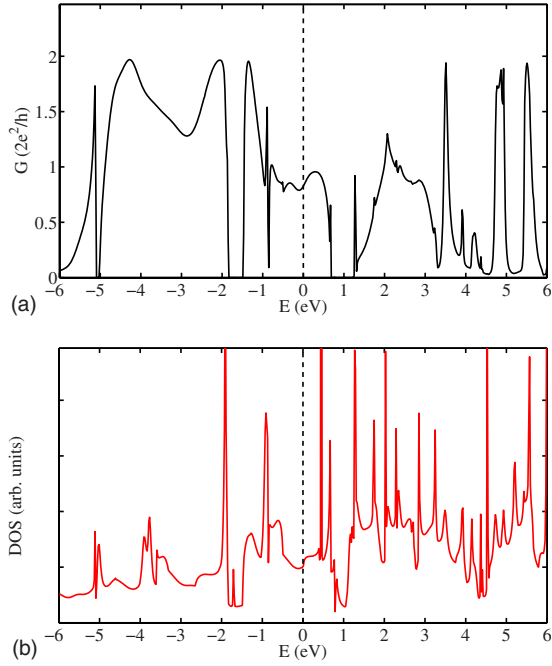


FIG. 5. (Color online) Electrical conductance (a) and DOS (b) of Al(001)-C₇-Al(001).

of nodes in Kohn-Sham eigenstates since the linear but complex combination of the latter ones forms the former conductance eigenchannel. Third, perfect phase oscillation on top of large $\rho_\alpha(\mathbf{x})$ lobes only happens near conductance maximum of $2G_0$ such as Figs. 6(a) and 6(b). Away from conductance maximum the eigenchannels, such as Figs. 6(c)–6(f), immediately exhibit more and more red and cyan isosurfaces at the left part of the conductor, suggesting that the incoming electron from the left lead is strongly scattered by the interface between Al(001) lead and carbon atomic chain. The reflected electrons cancel part of the forwarding phase oscillation at these energy levels. As a result, the right part of the conductor contains small portion of transmitted electrons which still display nontrivial phase gradient. These facts demonstrate the importance of both amplitude $\rho_\alpha(\mathbf{x})$ and phase gradient $\nabla\phi_\alpha(\mathbf{x})$ of probability current density.

If we read the conductance curve in Fig. 5(a) more carefully, there are gaps in the conductance curve, for example, $E \in [-1.8, -1.5]$ eV and $E \in [0.7, 1.2]$ eV. Such gaps are

TABLE I. Conductance eigenchannel decomposition of Al(001)-C₇-Al(001).

Label	Energy (eV)	Conductance (G_0)	Degeneracy
(a)	-4.27	0.984	2
(b)	-2.05	0.982	2
(c)	0.00	0.413	2
(d)	1.27	0.447	2
(e)	1.60	0.184	2
(f)	2.07	0.637	2
(g)	-1.71	0.003	2
(h)	0.77	0.003	2

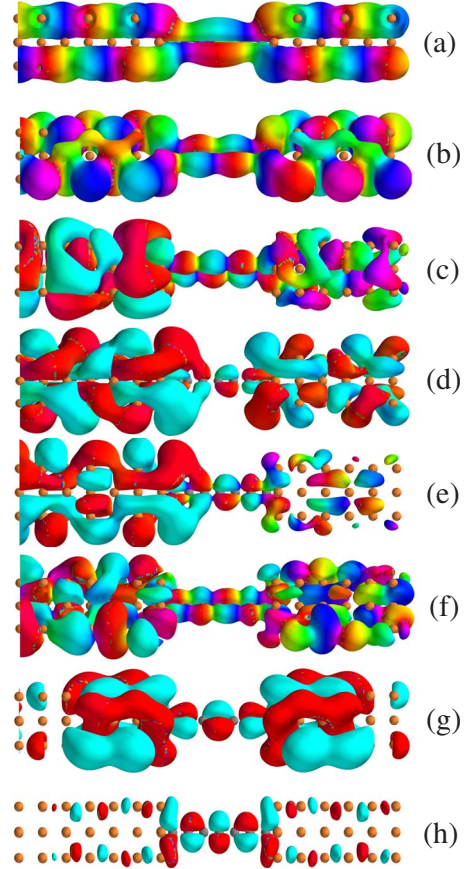


FIG. 6. (Color online) Phase-encoded conductance eigenchannels of Al(001)-C₇-Al(001) at different energy levels.

absent in pristine leads as shown in Fig. 4 and these small gaps are also absent in an infinite carbon chain. To understand the nature of these gaps, we focus on the first conductance gap at $[-1.8, -1.5]$ eV and plot the band structure of Al(001) lead in Fig. 8(a) as well as three conductance eigenchannels (A11, A12, and A13) at $E = -1.6$ eV in Fig. 8(b). A11, A12, and A13 clearly exhibit p_z , p_z , and d_{xy} characters, respectively. However, we have to emphasize that the d_{xy} character in the eigenchannel A13 is not directly from atomic d orbitals but from the linear combination of atomic s and p orbitals on each aluminum atom. Moreover, two p_x - and p_y - π conductance eigenchannels are found in infinite carbon atomic chain within the above energy region, so the transport gap is not due to nominal lack of states on the carbon. However, these two p_x and p_y π channels in the carbon chain have zero overlap with the above three eigenchannels (A11, A12, and A13) in the Al(001) lead due to difference symmetries. Therefore, the corresponding matrix element in the self-energy $\Sigma_{L,R}^r$ [Eqs. (8) and (9)] is zero, which leads to zero conductance. In another word, the above conductance gaps are demonstrations of a selection rule in phase-coherent quantum transport, that is, $G(E) = 0$ when

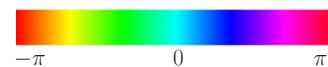


FIG. 7. (Color online) Colormap for quantum phase of conductance eigenchannels.

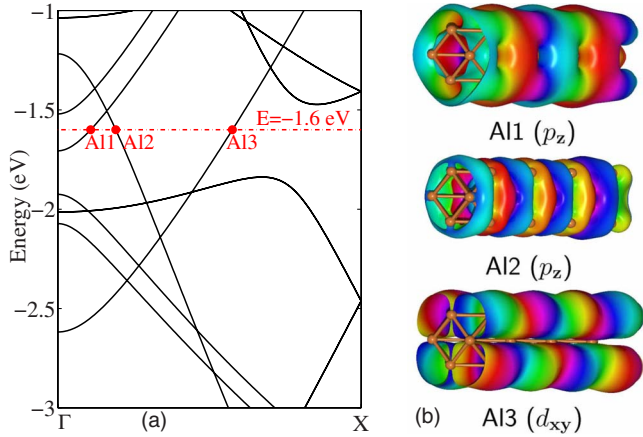


FIG. 8. (Color online) (a) Band structure of Al(001) lead and (b) three conductance eigenchannels in the pristine Al(001) lead at $E = -1.6$ eV. Phase amplitude is indicated by color using the colormap shown in Fig. 7.

$$\langle \psi_{L,R}(E) | \hat{H} | \psi_C(E) \rangle = 0 \quad (49)$$

at energy level E , where $\psi_{L,R}(E)$ and $\psi_C(E)$ are eigenchannels of the leads and the conductor.

A corresponding signature is also observed in the atomic-resolved projected DOS, shown in Fig. 9. Within the gap (except at $E = -1.71$ eV) the projected DOS on the carbon chain vanishes while the aluminum leads have non-negligible projected DOS of atomic s and p characters which can be seen from Fig. 3. We note that in addition to resonant transport, the incoming Al(001) band states could generally speaking induce two kinds of evanescent waves: one decaying rapidly through vacuum, and one decaying slowly in the carbon chain. Both kinds of evanescent waves could make the conductance in the gap not mathematically zero. Here, however, the second kind of evanescent waves is nonexistent because the p_z and d_{xy} eigenchannels in the Al(001) leads do not couple to the carbon chain's p_x and $p_y\pi$ orbitals at this energy region, and the carbon chain's $sp_z\sigma$ and σ^* states lie at energies far away, resulting in the vanishing coupling with the Al(001) p_z and d_{xy} state. The first kind of evanescent waves, which though exists mathematically, decay too rapidly in the vacuum region between two interfaces to have an actual effect on conductance. Therefore, the gap conductance can be taken to be literally zero.

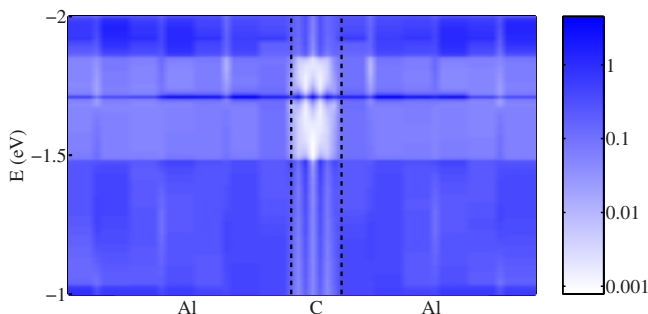


FIG. 9. (Color online) Atom-resolved projected DOS.

Strikingly, in Fig. 5(b) we also found within conductance gaps, there are sharp peaks in the DOS at $E = -1.71$ and 0.77 eV. We take the first peak at $E = -1.71$ eV as an example again. The sharp peak in the total DOS exactly corresponds to the narrow straight line in the atom-resolved projected DOS in Fig. 9, extending through both carbon chain and Al(001) leads. Conductance eigenchannel analysis further reveals that there exist two degenerate channels at $E = -1.71$ eV, however each of them contributes a very small conductance value of $0.003G_0$. The corresponding conductance eigenchannel, shown in Fig. 6(g), is a bound state, which is localized near the carbon atomic chain. It is very important to notice that the symmetry of this localized channel is also incompatible with the symmetry of Al1, Al2, and Al3 channels in Al(001) lead, therefore this localized channel should not carry any current according to the selection rule discussion above. It is in fact also an evanescent wave, starting from a discrete p_x and $p_y\pi$ state in the finite carbon chain and decaying exponentially into the semi-infinite Al(001) leads, since its eigenenergy falls into an energy gap in the subset of Al(001) band states which can couple to carbon's p_x and $p_y\pi$ state by symmetry. Because of the lack of coupling to Al(001) band states, this localized state (similar to donor level in semiconductors) is infinitely sharp in energy, and not smeared. The small numerical conductance comes from the numerical error due to the short leads used in the conductor, where the bound state formed between two interfaces does not completely vanish near the left and right boundaries of the conductor. We, therefore, did a separate calculation by adding four additional aluminum atomic layers to both sides of the present conductor, and the conductance indeed vanishes. This reminds us that in general unphysical conductance peaks may appear in conductance curves when the far end of the leads used in the setup of conductors is not long enough to resemble the true pristine lead. Furthermore, since electron density $\rho_\alpha(\mathbf{x})$ [Eq. (25)] of this bound state is large, the small conductance values can be only manifested in the small phase-gradient field $\nabla\phi_\alpha(\mathbf{x})$, leading to almost negligible phase-oscillation in the conductance eigenchannel shown in Fig. 6(g). Although $\nabla\phi_\alpha(\mathbf{x})$ is infinite in the transition zone between cyan (positive real) and red (negative real) lobes, $\rho_\alpha(\mathbf{x})$ is zero there. So it does not contribute to the current.

In addition, we would like to point out that the above bound state may become very important when finite bias voltage is applied. Electronic structure of the left and right leads will change with the bias voltage and symmetry-compatible conductance eigenchannels in the leads could be aligned close to the energy level of the bound state and have strong coupling with this state, forming a resonant tunneling channel. In this case, a Breit-Wigner conductance peak⁹⁵ with Lorentzian line shape is expected to appear in the conductance curve and contribute significantly to the total conductance. When the bias voltage further increases, symmetry-compatible conductance eigenchannels will be shifted away from the energy level of the bound state and the Breit-Wigner conductance peak will disappear. Correspondingly, the total conductance may drop substantially. Thus, in the current-voltage ($I-V$) curve one will observe a NDR region near the energy level of the bound state. The above

NDR characteristic shares exactly the same origin as the one found in resonant tunneling diodes^{96–98} in double barrier structures which were proposed and demonstrated in the early 1970s.

Finally, the detailed orbital hybridization between molecular orbitals of carbon atomic chain and surface states of two Al(001) leads can be directly identified from Fig. 6. Since under small bias the total current is determined by the conductance around the Fermi level, we take the eigenchannels in Fig. 6(c) at $E=0$ eV (or, the Fermi level) as an example. On the left surface layer, two $pp\sigma$ bonding orbitals are formed on two pairs of Al-Al bonds, which are further antibonded with each other, finally forming a surface state. This surface state is then *antibonded* with antibonding π^* state of carbon atomic chain. However, on the right end of carbon chain the antibonding π^* state forms a group of $pp\sigma$ bonding orbital with the p orbitals of four surface atoms on the right lead.

B. (4,4) CNT with substitutional silicon impurity

Atomic structure of (4,4) CNT with substitutional silicon impurity is presented in Fig. 10. The conductor is put inside a rectangular box of $13.512 \times 13.512 \times 19.607$ Å³ and electrons transport along the $+z$ direction. The left and right leads are formed by pristine (4,4) CNT with C-C bond length of 1.414 Å along the tube direction and C-C bond length of 1.399 Å perpendicular to the tube direction. Five atomic layers close to the silicon impurity are fully relaxed, resulting in two Si-C bonds along the tube direction with bond length of 1.780 Å and one Si-C bond perpendicular to the tube direction with bond length of 1.864 Å. DFT calculations are performed in the QUANTUM-ESPRESSO package using the PBE-GGA of exchange-correlation functional, a plane-wave basis with a cutoff of 340.0 eV, and ultrasoft pseudopotentials for both carbon and silicon atoms. Energy threshold E_{th} is set to 7.0 eV above the Fermi level for QO construction. Four QOs including one s and three p -like QOs are constructed for each silicon and carbon atom, shown in Fig. 11. The original AO characteristics are well preserved in QOs, meanwhile chemical environment due to the surrounding atoms clearly affects the detailed shapes.

Band structure, DOS, and electrical conductance of pristine (4,4) CNT are shown in Figs. 12(a) and 12(b). Two atomic layers are contained in a unit cell for both band structure and conductance calculations in the pristine (4,4) CNT, as indicated by dash lines in Fig. 10. *Ab initio* TB band structure (black-solid lines) using $R_{cut}=8$ Å is in a nice agreement with Kohn-Sham eigenvalues obtained from DFT calculation (red-filled dots) below $E=7.0$ eV. The black-open dots below $E=7.0$ eV are unbound states which exhibit little atomic characters, thus they are not used in the construction of QOs, hence are not meant to be reproduced by TB Hamiltonian. In the band structure plot two bands cross the Fermi level. This is reflected in the conductance curve of $2 G_0$ around the Fermi level in Fig. 12(b). Both steplike conductance curve and sharp DOS peaks near the edge of conductance steps are again found in pristine CNT(4,4).

Electrical conductance of (4,4) CNT with substitutional silicon impurity is shown in Fig. 13. First, conductance of

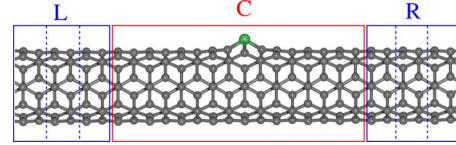


FIG. 10. (Color online) Atomic structure of (4,4) CNT with substitutional Si impurity. L: principal layer in the left lead; C: conductor; R: principal layer in the right lead. C: gray atoms; Si: green atom. Dashed lines in the left and right leads indicate the unit cell adopted for band structure and conductance calculations in the pristine (4,4) CNT.

the defect conductor is always lower than that of pristine CNT, demonstrating that maximum of conductance is controlled by the pristine CNT itself. Second, conductance of the original pristine CNT is affected considerably, but not completely destroyed. This is due to the fact that silicon and carbon share the same valence electronic structure, thus similar sp^2 bonds of Si-C and C-C are formed on the nanotube. Interestingly, a conductance dip is found near $E=0.6$ eV, indicating that silicon impurity atom and its induced structural relaxation indeed introduce some important difference from carbon atoms in CNT. To understand microscopic mechanism of this conductance dip, we carry out conductance eigenchannel analysis at five different energy levels, ranging from -1.0 to 1.1 eV. The corresponding conductance is listed in Table II. Two major eigenchannels are found for each energy levels. Conductance of channel 1, G_1 , is always

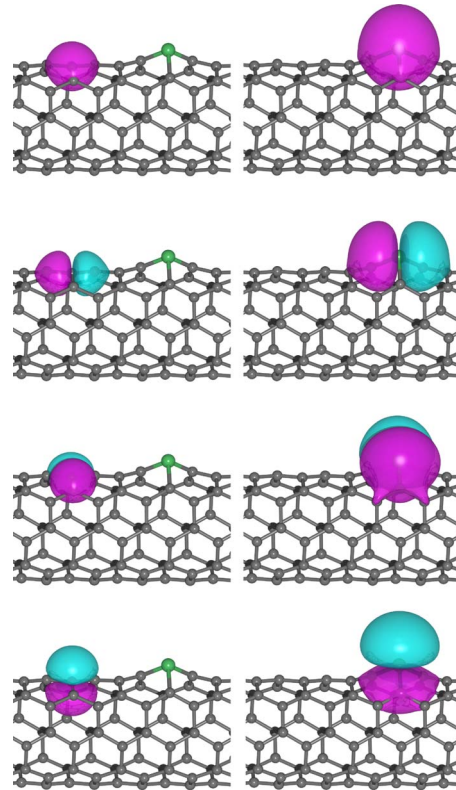


FIG. 11. (Color online) Quasiatomic orbitals in (4,4) CNT with substitutional Si impurity. Left (Right) column: s -, p_x -, p_y -, and p_z -like QOs on carbon (silicon) atom.

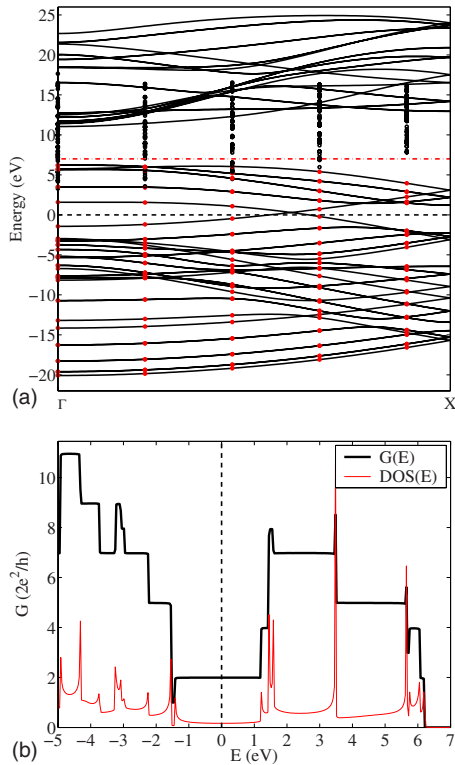


FIG. 12. (Color online) (a) Band structure (black-dashed line: the Fermi level; red dashed-dotted line: energy threshold; red-filled dots: DFT eigenvalues; black-open dots: DFT eigenvalues that are not used; black-solid lines: *ab initio* TB band structure) and (b) DOS (red-thin line) and electrical conductance (black-thick line) of pristine (4,4) CNT with $R_{\text{cut}}=8 \text{ \AA}$.

close to one quantum of conductance, thus is not influenced by the silicon impurity at all in the $[-1.0, 1.1] \text{ eV}$ energy range. On the other hand, conductance of channel 2, G_2 , changes dramatically. It varies from one quantum of conductance at $E=-1.0 \text{ eV}$ to almost zero at $E=0.6 \text{ eV}$, then to $0.77 G_0$ at $E=1.1 \text{ eV}$. To understand the mechanism, we plot the phase-encoded conductance eigenchannel in Fig. 14. It is clearly shown that channel 1 on the left column exhibits perfect phase oscillation from the left to the right of the conductor, suggesting almost negligible back-scattering in the presence of silicon impurity. However, channel 2 on the right column shows strong scattering near the silicon impurity when E is increased to 0.6 eV , displaying more red and cyan isosurfaces. At $E=0.6 \text{ eV}$, the incoming electron is completely reflected back, and forming evanescent wave, which carries vanishing current. When energy further increases away from 0.6 eV , the eigenchannel in Fig. 14(e) transmits nontrivial current again, showing clear phase oscillations in both ends of the conductor.

The phase-encoded conductance eigenchannels clearly reveal that the complete suppression of one conductance channel arises from destructive interference (antiresonance) when a discrete impurity state is coupled to the left and right continuum states, a particular scenario of the well-known Fano resonance^{99–101} when the asymmetry parameter approaches to zero. This phenomena has been observed in the previous first-principles studies of electron transport in CNTs by Choi

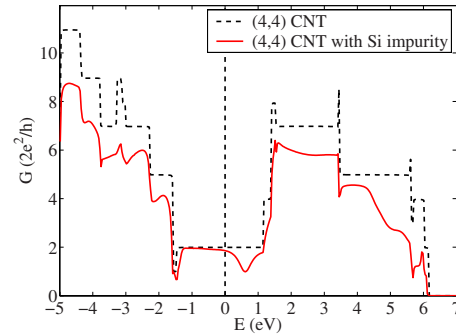


FIG. 13. (Color online) Electrical conductance of pristine (4,4) CNT (black-dash line) and (4,4) CNT with substitutional Si impurity (red-solid line).

*et al.*¹⁰² when (10,10) CNT contains boron and nitrogen impurities as well as carbon vacancies, Lee *et al.*⁷⁷ when (5,5) CNT is functionalized by small molecules through [2+1] cycloadditions, García-Lastra *et al.*¹⁰³ when single molecules are chemisorbed on (6,6) CNT, and Fürst *et al.*¹⁰⁴ when iron and vanadium adsorbed on (10,10) CNT. In general, the strength of effective scattering potential at the impurity has a pole at the Fano antiresonance energy.¹⁰¹ At this energy, the impurity becomes an infinite potential barrier to this channel despite the small size of the impurity atom relative to the eigenchannel wave function and completely reflects back the incoming wave. As a result, a standing-wave-like state is formed as the incoming wave is completely reflected back by the localized impurity state. This is exactly what we have observed at 0.6 eV in the second eigenchannel shown in Fig. 14(c), which contributes a very small conductance value of $0.002 G_0$. In addition, we have done a separate calculation near 0.6 eV using a finer energy grid and much smaller broadening parameter η . We found the conductance of the second channel indeed goes to zero at $E=0.6096 \text{ eV}$, in agreement with the Fano antiresonance model. Even though near 0.6 eV the conductance drop only happens to the second channel, it is expected that depending on the coupling strength the silicon impurity will introduce Fano antiresonance to the other conducting channels at different energies.

Interestingly, close to 0.6 eV both s - and p_z -like QOs of silicon impurity has significant contributions to projected DOS and eigenchannels while s -like QOs of carbon atoms away from silicon impurity has negligible contributions. Although silicon and carbon belong to the same group, the large size of silicon impurity introduces a strong structural deformation. Furthermore, carbon has higher electronegativ-

TABLE II. Conductance eigenchannel decomposition of (4,4) CNT with substitutional Si impurity.

Label	Energy (eV)	$G_1 (G_0)$	$G_2 (G_0)$
(a)	-1.00	0.993	0.963
(b)	0.00	0.990	0.867
(c)	0.37	0.989	0.513
(d)	0.60	0.987	0.002
(e)	1.10	0.990	0.771

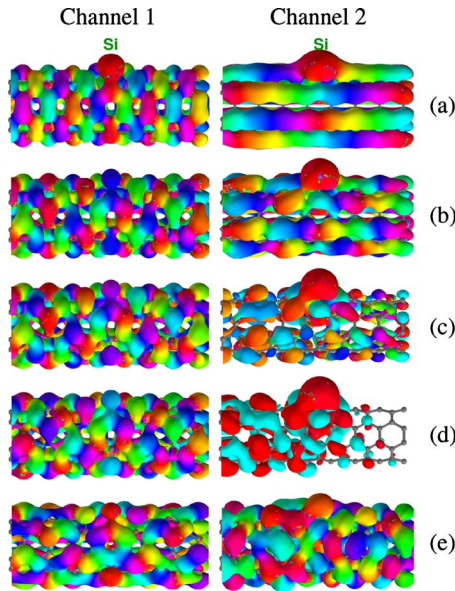


FIG. 14. (Color online) Phase-encoded conductance eigenchannels of (4,4) CNT with substitutional Si impurity at different energy levels. Phase amplitude is indicated by color using the color map shown in Fig. 7.

ity than silicon and electron will be more attracted to carbon atoms. Indeed QO-based Mulliken charge analysis indicates in (4,4) CNT silicon impurity loses 0.9 electron in total, which is equally distributed to its three nearest carbon neighbors. Both structural effect and electron density redistribution mentioned above push s and p_z states up to 0.6 eV above the Fermi level, which eventually leads to resonant suppression of transmission.

C. Benzene-1,4-dithiolate molecule between Au(111) metallic surfaces

Atomic structure of BDT molecule between Au(111) metallic surfaces is presented in Fig. 15, which is similar to the structure used by Strange *et al.*⁸⁰ The left and right leads are formed by perfect Au(111) surface with Au lattice constant of 4.180 Å, corresponding to Au-Au bond length of 2.956 Å. The principal layer is the same as the unit cell used in the ground-state DFT calculations, which contains 3×3 atoms in the surface plane and three layers of gold atoms along the transport direction ($+\hat{z}$). In the conductor, in order to reduce the effect of surface layer on the bulk leads we use six Au atomic layers in the left lead and seven Au atomic layers in the right lead, which are slightly different from those adopted by Strange *et al.* The distance between the surfaces of the left and right leads is 9.680 Å. The BDT molecule was initially placed at the hollow sites of Au(111) surface and only the BDT molecule in the conductor has been fully relaxed. As a result, $d_{\text{Au-S}}=2.436$ Å, $d_{\text{S-C}}=1.737$ Å, $d_{\text{C-C}}=1.401$ Å, and $d_{\text{C-H}}=1.089$ Å. The plane containing the BDT molecule is perpendicular to \hat{x} direction. Structural relaxation and ground-state DFT calculation are performed in the QUANTUM-ESPRESSO package using the PBE-GGA of exchange-correlation functional, ultra-

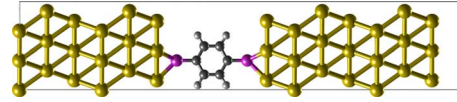


FIG. 15. (Color online) Atomic structure of Au(111)-BDT-Au(111) molecular junction.

soft pseudopotentials, and a plane-wave basis with a cutoff of 340.0 eV. We use 5×5 \mathbf{k} -point sampling along the transverse directions in the DFT calculation while nine irreducible ones of the total 25 \mathbf{k} points are adopted in the conductance calculation. Energy threshold E_{th} is set to 5.0 eV above the Fermi level for QO construction. Furthermore, one, four, four, and nine QOs are constructed for each H, C, S, and Au atom, respectively, corresponding to quasiatomic $\{s\}$, $\{s,p\}$, $\{s,p\}$, and $\{d,s,p\}$ characters. The representative QOs are shown in Fig. 16. It is again demonstrated that QOs generally inherit the original AO characters but the detail shapes are affected by their surrounding chemical environment.

The total conductance shown in Fig. 17 agrees very well with the conductance curve in Fig. 6 of Ref. 80. Particularly, zero-bias conductance at the Fermi level is $0.278 G_0$, in excellent agreement with $0.28 G_0$ by Strange *et al.* using MLWFs. However such agreement does not imply that QO and MLWF on top of ground-state DFT calculations can quantitatively describe quasiparticle transport properties. On the contrary, measured conductance in experiments is much smaller than the calculated ones.^{10,105-107} Beside geometric uncertainty and electron-phonon coupling effect in the experimental setup, this is largely due to the fact that quasiparticle energies and wave functions cannot be appropriately obtained from ground-state DFT. Therefore, it is very promising to use Hedin's GW approximation of quasi-particle energies and wave functions as the input of NEGF calculations, which can enlarge the energy gap between quasielectron and quasihole states and localize their associated wave functions, thus reducing the coupling strength, density of states, and total conductance at the Fermi level. Compared to the conductance curve using localized basis sets,⁸⁰ small difference is observed again including position and width of conductance peaks.

Electronic structure of the BDT molecule plays a critical role by providing a bridge for electron transport through the molecular junction. The BDT molecule embedded in the center of the conductor is directly coupled to the Au(111) surfaces, thus the molecular orbital energy levels could be strongly renormalized and orbital degeneracy may be lifted. A convenient way to study the above effects of local chemical environment is to project the total DOS onto fragment molecular orbital (FMO) which was proposed by Hoffmann¹⁰⁸ in the study of structural preferences of organometallic molecules. FMOs correspond to the eigenstates of TB Hamiltonian in the subspace of the fragment molecule \mathcal{M} that one is interested in,

$$|\text{FMO}_m\rangle = \sum_{ii \in \mathcal{M}} U_{ii,m}^{\mathcal{M}} |Q_{ii}\rangle, \quad (50)$$

where $\mathbf{U}^{\mathcal{M}}$ is a square matrix diagonalizing the Hamiltonian $H_{\mathcal{M}}$ with overlap matrix $O_{\mathcal{M}}$,

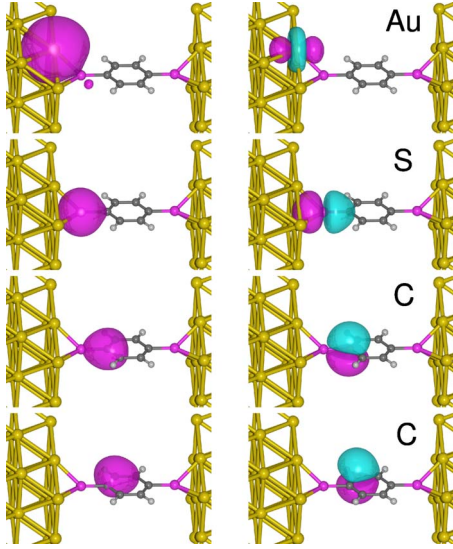


FIG. 16. (Color online) Quasiatomic orbitals in the Au(111)-BDT-Au(111) molecular junction. s and d_{z^2} for Au atom on the surface; s and p_z for S atom; and s and p_x for two C atoms.

$$\mathbf{H}^{\mathcal{M}}\mathbf{U}^{\mathcal{M}} = \mathbf{O}^{\mathcal{M}}\mathbf{U}^{\mathcal{M}}\boldsymbol{\epsilon}^{\mathcal{M}} \quad (51)$$

and it satisfies

$$[\mathbf{U}^{\mathcal{M}}]^\dagger \mathbf{O}^{\mathcal{M}} \mathbf{U}^{\mathcal{M}} = \mathbf{I}. \quad (52)$$

$\boldsymbol{\epsilon}^{\mathcal{M}}$ is a diagonal matrix whose m th diagonal element $\epsilon_m^{\mathcal{M}}$ is the renormalized energy level of $|\text{FMO}_m\rangle$. Their corresponding projected DOS can be easily obtained by projecting the eigenstates of the full Hamiltonian onto FMOs,

$$\rho_m^{\mathcal{M}}(E) = \sum_n |\langle \phi_n | \hat{S} | \text{FMO}_m \rangle|^2 \delta(E - \epsilon_n). \quad (53)$$

Figure 18 shows six π and π^* FMOs which originate from six p_x orbitals of the benzene molecule. The σ and σ^* FMOs are not shown here since we care more about the conductance close to the Fermi level where π and π^* FMOs are dominant. Compared to benzene in gas phase, the corresponding energy gap between FMO₃ and FMO₄ is reduced by more than 0.5 eV. Moreover, due to two S-C valence bonds the original doubly-degenerate HOMOs and LUMOs are split by 0.4 eV and 0.5 eV, respectively. The projected DOS of FMOs is presented in Fig. 19. We first notice that the projected DOS of the first three FMOs is mostly located below the Fermi level while the projected DOS of the other

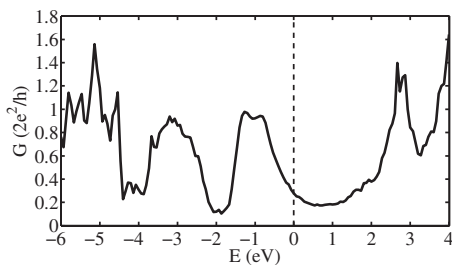


FIG. 17. Total electrical conductance of Au(111)-BDT-Au(111) molecular junction.

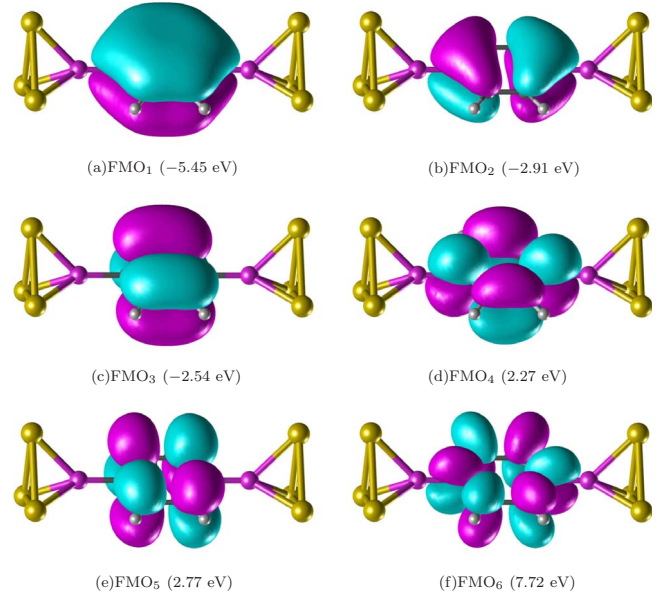


FIG. 18. (Color online) Six FMOs of benzene molecule in the Au(111)-BDT-Au(111) molecular junction at the Γ point of the first transverse Brillouin zone.

three FMOs is mostly located above the Fermi level, meaning that the fragment benzene molecule does not substantially donate or withdraw electrons from the rest of the conductor. Second, two sharp peaks are observed exactly at the energy levels of FMO₃ and FMO₅, indicating the absence of strong hybridization with sulfur atoms and Au(111) surfaces. In contrast to FMO₃ and FMO₅, the other four FMOs exhibit strong hybridization with sulfur atoms and Au(111) surfaces, leading to multiple peaks for each FMO in a wide range of energy centering around the energy level of the corresponding FMO.

More interestingly, comparing the conductance curve of Fig. 17 and projected DOS curve of Fig. 19, it seems there exists a clear correspondence between the broad conductance peaks and the projected DOS peaks, including $[-6, -4.5]$, $[-4, -2]$, $[-2, 0]$, and $[2, 3]$ eV. To have an unambiguous understanding of the role of FMO in the electron transport, we have carried out the conductance eigenchannel analysis in various peak regions, including five different energy levels, -5.1 , -3.0 , -1.0 , 0.0 , and 2.7 eV, at the Γ point of the first transverse Brillouin zone. We did not choose an energy level near FMO₆, simply because the energy threshold E_{th} for QO construction is set to 5.0 eV beyond which the electronic structure is not supposed to be accurately reproduced. It turns out that there exists only one dominating channel at the four higher energy levels, while at the lowest -5.1 eV there are two major conductance eigenchannels. Therefore, we plot in Fig. 20 the corresponding six conductance eigenchannels. Their conductance values are: $G_{\Gamma}(-5.1 \text{ eV}, 1) = 0.97 G_0$, $G_{\Gamma}(-5.1 \text{ eV}, 2) = 0.91 G_0$, $G_{\Gamma}(-3.0 \text{ eV}) = 0.52 G_0$, $G_{\Gamma}(-1.0 \text{ eV}) = 0.91 G_0$, and $G_{\Gamma}(0.0 \text{ eV}) = 0.41 G_0$, $G_{\Gamma}(2.7 \text{ eV}) = 0.16 G_0$. At -5.1 eV, two eigenchannels are almost perfectly conducting. The first one shown in Fig. 20(a) apparently exhibits σ character due to sp^2 hybridization. Whereas, the other five eigenchannels

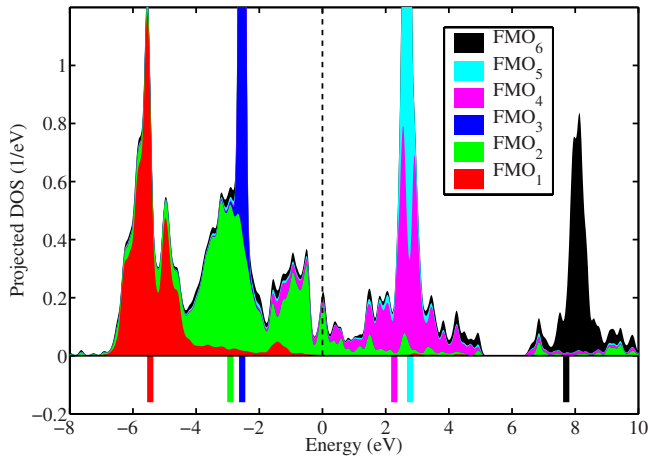


FIG. 19. (Color online) Projected DOS of benzene's six FMOs in the Au(111)-BDT-Au(111) molecular junction. The corresponding energy levels of FMO₁ to FMO₆ are marked as vertical lines from left to right below the projected DOS peaks.

shown in Figs. 20(b)–20(f) clearly resemble the characteristics of FMO₁, FMO₂, FMO₄, FMO₄, and FMO₅ in Fig. 18, respectively. The nearly perfect conductance eigenchannels in Figs. 20(a)–20(d) and their associated strong phase oscillations are the unambiguous evidence of resonant transport in the molecular junction through the π FMOs of benzene molecule. When energy moves away from the resonance, more and more backward scattering is introduced. Thus, at the Fermi level ($E_F=0.0$ eV) we observe less phase-oscillation in the left electrode and smaller transmitted electron probability density in the right electrode. In this case the conductance through off-resonant tunneling is only $0.41 G_0$.

In addition, Fig. 20 directly presents detailed chemical bonding information such as S-Au(111) and S-C₆H₄ in the conductance eigenchannels. For example, at -3.0 eV, near the left Au(111) surface p_x -QO on the sulfur atom and d -QOs on its nearest gold atoms form *bonding* orbitals, which is further *antibonded* with FMO₂ of benzene molecule whereas near the right surface FMO₂ forms *bonding* orbital with the sulfur atom's p_x -QO which is *antibonded* with d -QOs on the gold atoms. Such behavior changes when energy approaches to -1.0 eV. On the left surface *antibonding* character becomes clear between d -QOs on the sulfur's nearest gold atoms and p_x -QO on the sulfur atom while the latter one forms *bonding* orbital with benzene's FMO₄ orbital. A similar situation is observed on the right-hand side.

In conclusion, the conductance eigenchannel analysis together with the FMO analysis evidently demonstrates that single molecule can become perfectly conducting at appropriate energy levels via resonant tunneling through molecular orbitals of single molecules.

V. SUMMARY

In summary, we have developed Green's-function method within the Landauer-Büttiker formalism for phase-coherent quantum transport using recently developed *ab initio* QOs and the corresponding *ab initio* TB Hamiltonian and overlap

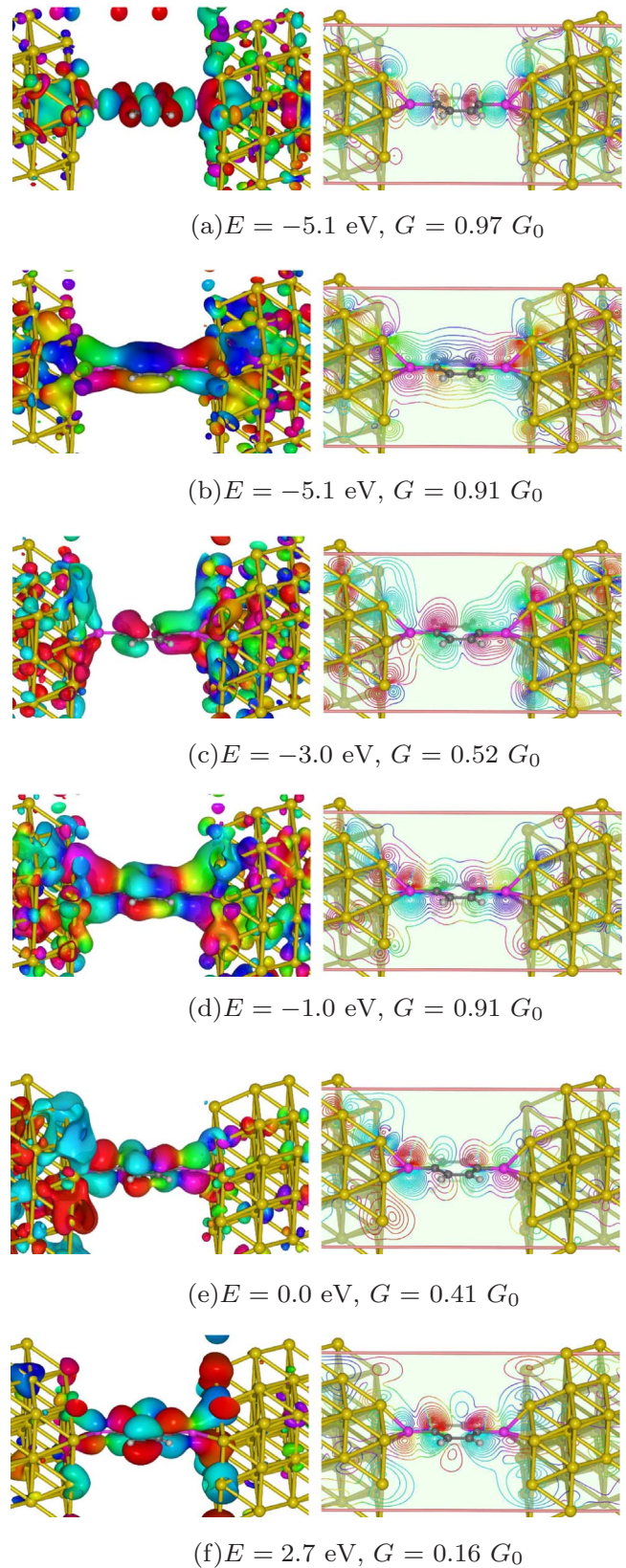


FIG. 20. (Color online) Phase-encoded conductance eigenchannels and their corresponding energy level and conductance in the Au(111)-BDT-Au(111) molecular junction at the Γ point of the first transverse Brillouin zone. Phase amplitude is indicated by color using the color map shown in Fig. 7.

matrices. QOs are efficiently and robustly constructed in the spirit of LCAO by maximizing the total sum-of-square measure of pseudoatomic orbitals projected onto Kohn-Sham eigenstates. Thanks to resolution of the identity, no explicit high-lying eigenstates are required for QO construction, which dramatically reduces computation load and memory requirement. QOs, on one hand, preserve the original AO characteristics and are highly localized around atoms, thus can be easily identified and interpreted. On the other hand, electronic structure, such as band structure, DOS, and Fermi surface, can be accurately reproduced using the corresponding TB Hamiltonian and overlap matrices. QOs, therefore, can serve as *ab initio* minimal basis in Green's-function method for studying phase-coherent quantum transport, which we have briefly formulated for two-terminal devices within the Landauer-Büttiker formalism.

We have demonstrated both efficiency and robustness of our approach by three studies of standard two-terminal devices. In the case of Al(001)-C₇-Al(001), electrical conductance agrees very well with other calculations using localized basis set while slight difference is observed near the Fermi level and conductance edges. Our conductance eigenchannel analysis has shown that the conductance near the Fermi level is fully controlled by doubly-degenerate π channels through carbon atomic chain, hybridized with surface states from the left and right aluminum contacts. Perfect phase oscillation was found at the conductance maximum of $2 G_0$ only, displaying negligible back-scattering at the interface between atomic chain and aluminum leads. Away from the energy levels of conductance maximum, two gaps are found in the conductance curves. We have shown that they arise from the selection rule with the vanishing Hamiltonian and overlap matrix elements between symmetry-incompatible eigenchannels in the aluminum leads and carbon atomic chain and quantum tunneling of the evanescent waves between two distant interfaces contribute negligible conductance. In the second application, we studied phase-coherent transport in (4,4) CNT with a substitutional silicon impurity. The conductance close to the Fermi level is determined by two eigenchannels, one of which is unaffected by the impurity, whereas in the other one the incoming electrons are completely reflected at

$E=0.6$ eV. The complete suppression of transmission at 0.6 eV in one of the two conductance eigenchannels is attributed to the destructive Fano antiresonance when the localized silicon impurity state couples with the continuum states of carbon nanotube. In the third application, we applied our approach to a more complicated system where a BDT molecule is attached to the hollow sites of two Au(111) surfaces. In this case, \mathbf{k} -point sampling in the transverse Brillouin zone was adopted. Combining fragment molecular orbital analysis and conductance eigenchannel analysis, we have shown that at certain energy levels the single-molecule BDT when attached to Au(111) surfaces become perfectly conducting via resonant tunneling transport through benzene's σ and π fragment molecular orbitals. Our conductance curve is in excellent agreement with the one obtained from Green's-function calculation in the MLWF basis.⁸⁰ On the other hand, compared to the conductance curve using localized basis sets, slight difference is also observed including position and width of conductance peaks. Therefore, although in general NEGF in localized basis sets can provide accurate conductance curves, more attention has to be paid to choosing appropriate localized basis sets in order to achieve both accuracy and efficiency. Relevant information of the program and the above calculations is placed at a publicly accessible website.⁸³

Our studies demonstrate that conductance eigenchannel analysis facilitates the understanding of microscopic transport mechanism and could be important for designing future molecular and nanoscale electronic devices. It is straightforward to extend the present approach to NEGF method in the *ab initio* QO basis set in order to analyze devices in nonequilibrium conditions and this work is currently under way.

ACKNOWLEDGMENTS

This work was supported by the Director for Energy Research and Office of Basic Energy Sciences. J.L. acknowledges support by NSF MRSEC under Grant No. DMR-0520020 and AFOSR under Grant No. FA9550-08-1-0325. We thank Cai-Zhuang Wang, Kai-Ming Ho, and Clemens Först for valuable discussions.

*Author to whom correspondence should be addressed; qianxf@alum.mit.edu

¹C. Joachim, J. K. Gimzewski, and A. Aviram, *Nature (London)* **408**, 541 (2000).

²A. Nitzan, *Annu. Rev. Phys. Chem.* **52**, 681 (2001).

³P. Avouris, *Acc. Chem. Res.* **35**, 1026 (2002).

⁴J. R. Heath and M. A. Ratner, *Phys. Today* **56**(5), 43 (2003).

⁵A. Nitzan and M. A. Ratner, *Science* **300**, 1384 (2003).

⁶C. Joachim and M. A. Ratner, *Proc. Natl. Acad. Sci. U.S.A.* **102**, 8801 (2005).

⁷N. J. Tao, *Nat. Nanotechnol.* **1**, 173 (2006).

⁸S. M. Lindsay and M. A. Ratner, *Adv. Mater.* **19**, 23 (2007).

⁹A. Aviram and M. A. Ratner, *Chem. Phys. Lett.* **29**, 277 (1974).

¹⁰M. A. Reed, C. Zhou, C. J. Muller, T. P. Burgin, and J. M. Tour,

Science **278**, 252 (1997).

¹¹R. H. M. Smit, Y. Noat, C. Untiedt, N. D. Lang, M. C. van Hemert, and J. M. van Ruitenbeek, *Nature (London)* **419**, 906 (2002).

¹²M. T. González, S. M. Wu, R. Huber, S. J. van der Molen, C. Schonenberger, and M. Calame, *Nano Lett.* **6**, 2238 (2006).

¹³E. Lörtscher, H. B. Weber, and H. Riel, *Phys. Rev. Lett.* **98**, 176807 (2007).

¹⁴B. Q. Xu and N. J. J. Tao, *Science* **301**, 1221 (2003).

¹⁵S. Y. Jang, P. Reddy, A. Majumdar, and R. A. Segalman, *Nano Lett.* **6**, 2362 (2006).

¹⁶L. Venkataraman, J. E. Klare, I. W. Tam, C. Nuckolls, M. S. Hybertsen, and M. L. Steigerwald, *Nano Lett.* **6**, 458 (2006).

¹⁷J. He, F. Chen, S. Lindsay, and C. Nuckolls, *Appl. Phys. Lett.*

- 90**, 072112 (2007).
- ¹⁸Z. H. Li, I. Pobelov, B. Han, T. Wandlowski, A. Blaszczyk, and M. Mayor, *Nanotechnology* **18**, 044018 (2007).
 - ¹⁹W. Haiss, R. J. Nichols, H. van Zalinge, S. J. Higgins, D. Bethell, and D. J. Schiffrin, *Phys. Chem. Chem. Phys.* **6**, 4330 (2004).
 - ²⁰H. van Zalinge, D. J. Schiffrin, A. D. Bates, E. B. Starikov, W. Wenzel, and R. J. Nichols, *Angew. Chem., Int. Ed.* **45**, 5499 (2006).
 - ²¹R. Landauer, *IBM J. Res. Dev.* **1**, 223 (1957).
 - ²²M. Büttiker, Y. Imry, R. Landauer, and S. Pinhas, *Phys. Rev. B* **31**, 6207 (1985).
 - ²³M. Büttiker, *Phys. Rev. Lett.* **57**, 1761 (1986).
 - ²⁴Y. C. Chen, M. Zwolak, and M. Di Ventra, *Nano Lett.* **3**, 1691 (2003).
 - ²⁵T. Frederiksen, M. Brandbyge, N. Lorente, and A. P. Jauho, *Phys. Rev. Lett.* **93**, 256601 (2004).
 - ²⁶N. Sergueev, D. Roubtsov, and H. Guo, *Phys. Rev. Lett.* **95**, 146803 (2005).
 - ²⁷T. Frederiksen, M. Paulsson, M. Brandbyge, and A. P. Jauho, *Phys. Rev. B* **75**, 205413 (2007).
 - ²⁸M. Tsutsui, M. Taniguchi, and T. Kawai, *Nano Lett.* **8**, 3293 (2008).
 - ²⁹M. Galperin, M. A. Ratner, and A. Nitzan, *Nano Lett.* **5**, 125 (2005).
 - ³⁰M. Galperin, A. Nitzan, M. A. Ratner, and D. R. Stewart, *J. Phys. Chem. B* **109**, 8519 (2005).
 - ³¹Y. Meir and N. S. Wingreen, *Phys. Rev. Lett.* **68**, 2512 (1992).
 - ³²A. Ferretti, A. Calzolari, R. Di Felice, F. Manghi, M. J. Caldas, M. Buongiorno Nardelli, and E. Molinari, *Phys. Rev. Lett.* **94**, 116802 (2005).
 - ³³A. Ferretti, A. Calzolari, R. Di Felice, and F. Manghi, *Phys. Rev. B* **72**, 125114 (2005).
 - ³⁴S. Datta, *Electronic Transport in Mesoscopic Systems* (Cambridge University Press, Cambridge, 1995).
 - ³⁵M. Buongiorno Nardelli, *Phys. Rev. B* **60**, 7828 (1999).
 - ³⁶P. A. Derosa and J. M. Seminario, *J. Phys. Chem. B* **105**, 471 (2001).
 - ³⁷P. S. Damle, A. W. Ghosh, and S. Datta, *Phys. Rev. B* **64**, 201403 (2001).
 - ³⁸J. Taylor, H. Guo, and J. Wang, *Phys. Rev. B* **63**, 245407 (2001).
 - ³⁹B. Larade, J. Taylor, H. Mehrez, and H. Guo, *Phys. Rev. B* **64**, 075420 (2001).
 - ⁴⁰Y. Q. Xue, S. Datta, and M. A. Ratner, *Chem. Phys.* **281**, 151 (2002).
 - ⁴¹M. Brandbyge, J. L. Mozos, P. Ordejon, J. Taylor, and K. Stokbro, *Phys. Rev. B* **65**, 165401 (2002).
 - ⁴²J. J. Palacios, A. J. Pérez-Jiménez, E. Louis, E. SanFabián, and J. A. Vergés, *Phys. Rev. B* **66**, 035322 (2002).
 - ⁴³J. J. Palacios, A. J. Pérez-Jiménez, E. Louis, E. SanFabián, and J. A. Vergés, *Phys. Rev. Lett.* **90**, 106801 (2003).
 - ⁴⁴K. Stokbro, J. Taylor, M. Brandbyge, and P. Ordejon, *Ann. N.Y. Acad. Sci.* **1006**, 212 (2003).
 - ⁴⁵Y. Q. Xue and M. A. Ratner, *Phys. Rev. B* **68**, 115406 (2003).
 - ⁴⁶S. H. Ke, H. U. Baranger, and W. T. Yang, *Phys. Rev. B* **70**, 085410 (2004).
 - ⁴⁷S. Datta, *Quantum Transport: Atom to Transistor* (Cambridge University Press, Cambridge, 2005).
 - ⁴⁸N. D. Lang, *Phys. Rev. B* **52**, 5335 (1995).
 - ⁴⁹K. Hirose and M. Tsukada, *Phys. Rev. B* **51**, 5278 (1995).
 - ⁵⁰N. Kobayashi, M. Brandbyge, and M. Tsukada, *Phys. Rev. B* **62**, 8430 (2000).
 - ⁵¹H. J. Choi and J. Ihm, *Phys. Rev. B* **59**, 2267 (1999).
 - ⁵²M. Di Ventra and N. D. Lang, *Phys. Rev. B* **65**, 045402 (2001).
 - ⁵³A. Smogunov, A. Dal Corso, and E. Tosatti, *Phys. Rev. B* **70**, 045417 (2004).
 - ⁵⁴H. J. Choi, M. L. Cohen, and S. G. Louie, *Phys. Rev. B* **76**, 155420 (2007).
 - ⁵⁵J. M. MacLaren, X. G. Zhang, W. H. Butler, and X. D. Wang, *Phys. Rev. B* **59**, 5470 (1999).
 - ⁵⁶P. Hohenberg and W. Kohn, *Phys. Rev.* **136**, B864 (1964).
 - ⁵⁷W. Kohn and L. J. Sham, *Phys. Rev.* **140**, A1133 (1965).
 - ⁵⁸L. Hedin, *Phys. Rev.* **139**, A796 (1965).
 - ⁵⁹J. B. Neaton, M. S. Hybertsen, and S. G. Louie, *Phys. Rev. Lett.* **97**, 216405 (2006).
 - ⁶⁰S. Y. Quek, J. B. Neaton, M. S. Hybertsen, E. Kaxiras, and S. G. Louie, *Phys. Rev. Lett.* **98**, 066807 (2007).
 - ⁶¹K. S. Thygesen and A. Rubio, *J. Chem. Phys.* **126**, 091101 (2007).
 - ⁶²E. Runge and E. K. U. Gross, *Phys. Rev. Lett.* **52**, 997 (1984).
 - ⁶³G. Stefanucci and C.-O. Almbladh, *Europhys. Lett.* **67**, 14 (2004).
 - ⁶⁴K. Burke, R. Car, and R. Gebauer, *Phys. Rev. Lett.* **94**, 146803 (2005).
 - ⁶⁵N. Bushong, N. Sai, and M. Di Ventra, *Nano Lett.* **5**, 2569 (2005).
 - ⁶⁶X. F. Qian, J. Li, X. Lin, and S. Yip, *Phys. Rev. B* **73**, 035408 (2006).
 - ⁶⁷C. L. Cheng, J. S. Evans, and T. Van Voorhis, *Phys. Rev. B* **74**, 155112 (2006).
 - ⁶⁸J. C. Slater and G. F. Koster, *Phys. Rev.* **94**, 1498 (1954).
 - ⁶⁹W. J. Ehre, R. F. Stewart, and J. A. Pople, *J. Chem. Phys.* **51**, 2657 (1969).
 - ⁷⁰J. Junquera, O. Paz, D. Sanchez-Portal, and E. Artacho, *Phys. Rev. B* **64**, 235111 (2001).
 - ⁷¹T. Ozaki, *Phys. Rev. B* **67**, 155108 (2003).
 - ⁷²N. Marzari and D. Vanderbilt, *Phys. Rev. B* **56**, 12847 (1997).
 - ⁷³I. Souza, N. Marzari, and D. Vanderbilt, *Phys. Rev. B* **65**, 035109 (2001).
 - ⁷⁴J. M. Foster and S. F. Boys, *Rev. Mod. Phys.* **32**, 300 (1960).
 - ⁷⁵A. Calzolari, N. Marzari, I. Souza, and M. Buongiorno Nardelli, *Phys. Rev. B* **69**, 035108 (2004).
 - ⁷⁶Y. S. Lee, M. Buongiorno Nardelli, and N. Marzari, *Phys. Rev. Lett.* **95**, 076804 (2005).
 - ⁷⁷Y. S. Lee and N. Marzari, *Phys. Rev. Lett.* **97**, 116801 (2006).
 - ⁷⁸K. S. Thygesen, L. B. Hansen, and K. W. Jacobsen, *Phys. Rev. Lett.* **94**, 026405 (2005).
 - ⁷⁹K. S. Thygesen and K. W. Jacobsen, *Chem. Phys.* **319**, 111 (2005).
 - ⁸⁰M. Strange, I. S. Kristensen, K. S. Thygesen, and K. W. Jacobsen, *J. Chem. Phys.* **128**, 114714 (2008).
 - ⁸¹X. F. Qian, J. Li, L. Qi, C. Z. Wang, T. L. Chan, Y. X. Yao, K. M. Ho, and S. Yip, *Phys. Rev. B* **78**, 245112 (2008).
 - ⁸²W. C. Lu, C. Z. Wang, T. L. Chan, K. Ruedenberg, and K. M. Ho, *Phys. Rev. B* **70**, 041101 (2004).
 - ⁸³Quasiatomic orbitals for transport, QOT, <http://alum.mit.edu/www/qianxf/QOT>
 - ⁸⁴D. H. Lee and J. D. Joannopoulos, *Phys. Rev. B* **23**, 4988 (1981).
 - ⁸⁵M. P. L. Sancho, J. M. L. Sancho, and J. Rubio, *J. Phys. F: Met.*

- Phys. **14**, 1205 (1984).
- ⁸⁶M. P. L. Sancho, J. M. L. Sancho, and J. Rubio, *J. Phys. F: Met. Phys.* **15**, 851 (1985).
- ⁸⁷M. P. L. Sancho, J. M. L. Sancho, and J. Rubio, *J. Phys. C* **18**, 1803 (1985).
- ⁸⁸M. Paulsson and M. Brandbyge, *Phys. Rev. B* **76**, 115117 (2007).
- ⁸⁹The persistence of vision raytracer, POV-RAY, <http://www.povray.org>
- ⁹⁰<http://cms.mpi.univie.ac.at/vasp/>, VASP.
- ⁹¹<https://wiki.fysik.dtu.dk/dacapo>, DACAPO.
- ⁹²P. Giannozzi *et al.*, *J. Phys.: Condens. Matter* **21**, 395502 (2009).
- ⁹³J. P. Perdew, K. Burke, and M. Ernzerhof, *Phys. Rev. Lett.* **77**, 3865 (1996).
- ⁹⁴D. Vanderbilt, *Phys. Rev. B* **41**, 7892 (1990).
- ⁹⁵G. Breit and E. Wigner, *Phys. Rev.* **49**, 519 (1936).
- ⁹⁶R. Tsu and L. Esaki, *Appl. Phys. Lett.* **22**, 562 (1973).
- ⁹⁷L. L. Chang, L. Esaki, and R. Tsu, *Appl. Phys. Lett.* **24**, 593 (1974).
- ⁹⁸T. C. L. G. Sollner, W. D. Goodhue, P. E. Tannenwald, C. D. Parker, and D. D. Peck, *Appl. Phys. Lett.* **43**, 588 (1983).
- ⁹⁹U. Fano, *Phys. Rev.* **124**, 1866 (1961).
- ¹⁰⁰X. R. Wang, Yupeng Wang, and Z. Z. Sun, *Phys. Rev. B* **65**, 193402 (2002).
- ¹⁰¹A. E. Miroshnichenko, S. Flach, and Y. S. Kivshar, *Rev. Mod. Phys.* **82**, 2257 (2010).
- ¹⁰²H. J. Choi, J. Ihm, S. G. Louie, and M. L. Cohen, *Phys. Rev. Lett.* **84**, 2917 (2000).
- ¹⁰³J. M. García-Lastra, K. S. Thygesen, M. Strange, and A. Rubio, *Phys. Rev. Lett.* **101**, 236806 (2008).
- ¹⁰⁴J. A. Fürst, M. Brandbyge, A. P. Jauho, and K. Stokbro, *Phys. Rev. B* **78**, 195405 (2008).
- ¹⁰⁵X. Y. Xiao, B. Q. Xu, and N. J. Tao, *Nano Lett.* **4**, 267 (2004).
- ¹⁰⁶S. Ghosh, H. Halimun, A. K. Mahapatro, J. Choi, S. Lodha, and D. Janes, *Appl. Phys. Lett.* **87**, 233509 (2005).
- ¹⁰⁷J. Ulrich, D. Esrail, W. Pontius, L. Venkataraman, D. Millar, and L. H. Doerrer, *J. Phys. Chem. B* **110**, 2462 (2006).
- ¹⁰⁸R. Hoffmann, *Science* **211**, 995 (1981).